2 MODULATION OF A WAVE FRONT WITH A LCSLM

2.1 Models for the twisted nematic cell

There has been a massive effort beginning in the seventies to bring out liquid crystals with better performance, mainly because of their display applications. At the same time different display modes have been investigated, among them the twisted nematic cell (TN-cell) has become the most extended one.

In order to analyze and study the optical performance of the liquid crystal devices we need to know the orientation of the molecular director $\vec{n}$ across the cell. This orientation can be calculated through a direct approach or through a reverse-engineering approach. In the direct approach, the designers of liquid crystal devices calculate the exact orientation of the molecular director $\vec{n}$ by applying the elastic and electromagnetic theory, and by using the values for the parameters of the LC molecules and the LC cell. Normally the users of LC devices do not have access to the values of these parameters. Then a reverse-

engineering process is required to calculate by means of indirect measurements and using simple models the distribution of the molecular director $\vec{n}$ across the cell. In this sense different models have been proposed for the TN-cells [Lu90,Coy96] but they show a lack of accuracy. Recently we proposed a simplified model [PAPER A] that not only provides a good estimation but also permits a quantitative prediction of the optical performance of the TN-cell, thus bridging the gap between exact and inverse approaches. We note that in the following we will concentrate our attention on the TN-cell, even though some results may also be applied to other LC display modes. The exact description provided by the direct approach is presented in Section 2.2.1. In Section 2.2.2 we derive the model proposed in this thesis and presented in [PAPER A]. We illustrate that the previous models used in the reverse-engineering approach can be considered as particular cases of the new model we propose.

2.1.1 Direct approach: exact description

In the direct approach the researcher knows the values of the physical parameters of the liquid crystal molecules. If the steady-state directors distribution is to be calculated, the necessary parameters are the elastic constants and the dielectric anisotropy $\boldsymbol{De} = \boldsymbol{e}_{\parallel} - \boldsymbol{e}_{\wedge}$. If calculating the dynamic response of the LC directors the values for the viscosity coefficients are also necessary. In this thesis our interest is focused on the steady-state performance of the TN-cell.

In Section 1.2.1 we mentioned the elastic constants k_{11}, k_{22}, k_{33} for the splay, the twist, and the bend deformations of the liquid crystals respectively. We consider that the deformations in the TN-cell are produced at constant temperature and at constant pressure. The expression for the elastic free energy density U_L is derived from the Oseen-Frank elastic theory that in the case of the TN-cell [Yeh99] provides

$$U_L = \frac{1}{2}\left(k_{11}\cos^2\boldsymbol{q} + k_{33}sin^2\boldsymbol{q}\right)\left(\frac{d\boldsymbol{q}}{dz}\right)^2 + \frac{1}{2}\left(k_{22}\cos^2\boldsymbol{q} + k_{33}sin^2\boldsymbol{q}\right)\cos^2\boldsymbol{q}\left(\frac{d\boldsymbol{c}}{dz}\right)^2 \quad (2\text{-}1)$$

where z is the coordinate along the twist axis. $\boldsymbol{c}$ and $\boldsymbol{q}$ are respectively the twist and the tilt angles shown in Figure 1.2, which determine the distribution of the molecular director $\vec{n}$ in the cell.

When an electric field $\vec{E}$ is applied to a material, the macroscopic electrostatic free energy density U_E is given by

$$U_E = \tfrac{1}{2}\vec{D}\cdot\vec{E} \tag{2-2}$$

where $\vec{D}$ is the displacement field vector. The dielectric permittivity relates the displacement field vector $\vec{D}$ and the applied electric field $\vec{E}$, $\vec{D}=\boldsymbol{e}\,\vec{E}$. In an anisotropic electric material, as the nematic liquid crystal, the dielectric permittivity $\boldsymbol{e}$ is a tensorial magnitude. Taking this into account, under an applied electric field along the Z axis the electromagnetic energy density U_E in a TN-cell can be written as [Yeh99]

$$U_E = \frac{1}{2}\frac{D_z{}^2}{\boldsymbol{e}_{\parallel}\sin^2\boldsymbol{q}+\boldsymbol{e}_{\perp}\cos^2\boldsymbol{q}} \tag{2-3}$$

As explained in Section 1.2.1, the external surfaces (planes $z=0$ and $z=d$) are coated with an alignment layer in order to force the molecular director to lay along the surfaces, pointing in a specific direction. The anchoring of the LC molecules at the surfaces imposes a boundary condition to the free movement of the LC molecules in the TN-cell. In order to find the distribution of the director $\vec{n}$ across the cell we have to minimize the total free energy of the cell U,

$$U = \int_0^d \left(U_L + U_E\right)dz \tag{2-4}$$

This minimization, $\boldsymbol{d}U = 0$, requires the technique of variational calculus.

When there is no voltage applied, field-off state, only the elastic free energy density U_L contributes to the total free energy U. From the minimum free energy condition $\boldsymbol{d}U = 0$ we obtain the tilt angle $\boldsymbol{q}$ as constant and equal to 90 degrees, i.e. the director axis is perpendicular to the twist axis all along the cell

[Gen93]. Furthermore, the twist c is linear with respect to the cell thickness z, that is $c = a\,z/d$, where a is the total twist angle and d is the total cell thickness, also called cell gap. In Figure 2.1 the twist and the tilt evolutions are represented as a function of the cell depth z.
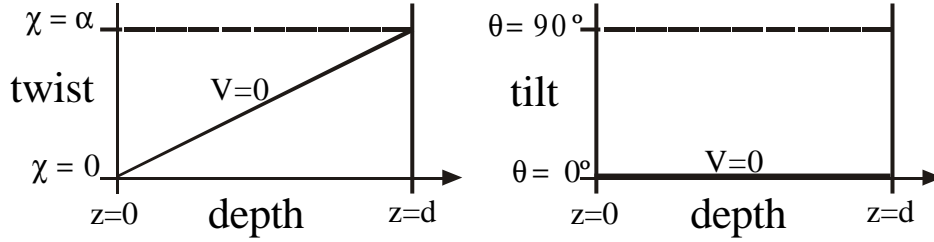

Figure 2.1. Profiles for the twist c and the tilt q angles in the field-off state.

Using this description, and applying the Jones matrix formalism for polarized light, Yariv and Yeh [Yar84] derived the expression for the Jones matrix of the TN-cell in the field-off state. They regarded the TN-cell as a stack of uniaxial birefringent layers, each one slightly twisted with respect to the previous one. As a result of the matrix product of the different layers they obtained an analytical expression for the Jones matrix of the TN-cell, in the following denoted as M_{LCSLM},

$$M_{LCSLM}\,(\boldsymbol{a}, \boldsymbol{b}) = exp(-i\boldsymbol{b})\ R(-\boldsymbol{a})\ M(\boldsymbol{a}, \boldsymbol{b}) \tag{2-5}$$

We note that this expression depends on the total twist angle $\boldsymbol{a}$ and on the birefringence $\boldsymbol{b}$ of the TN-cell. As we commented in Section 1.2.1, we use the definition for birefringence typically found in the literature related with LCDs and LCSLMs. In Eq. (2-5), $R(\boldsymbol{v})$ is the 2×2 rotation matrix (for a generic angle $\boldsymbol{v}$),

$$R(\boldsymbol{v}) = \begin{pmatrix} cos\,\boldsymbol{v} & sin\,\boldsymbol{v} \\ -sin\,\boldsymbol{v} & cos\,\boldsymbol{v} \end{pmatrix} \tag{2-6}$$

and the matrix $M(\boldsymbol{a}, \boldsymbol{b})$ is given by

$$M(\boldsymbol{a}, \boldsymbol{b}) = \begin{pmatrix} X - iY & Z \\ -Z & X + iY \end{pmatrix} \tag{2-7}$$

where

$$X = cos\,\boldsymbol{g} \qquad\qquad (2\text{-}8a)$$

$$Y = \frac{\boldsymbol{b}}{\boldsymbol{g}} sin\,\boldsymbol{g} \qquad\qquad (2\text{-}8b)$$

$$Z = \frac{\boldsymbol{a}}{\boldsymbol{g}} sin\,\boldsymbol{g} \qquad\qquad (2\text{-}8c)$$

$\boldsymbol{g} = \sqrt{\boldsymbol{a}^2 + \boldsymbol{b}^2}$ is a parameter that combines the twist $\boldsymbol{a}$ and the birefringence $\boldsymbol{b}$ of the TN-LCSLM. The notation X,Y,Z for the elements in the Jones matrix of the TN-LCSLM was introduced in [Bou97].

In the presence of an applied voltage V, there is a competition between the consequent electric torque and the elastic restoring torque imposed by the anchoring at the surfaces. At first, as the applied voltage increases in magnitude, there is no change in the orientation of the director $\vec{n}$ with respect to the field-off state situation. However, when the applied voltage exceeds the Freedericksz transition threshold V_{th}, the molecular director changes its orientation from one molecule to the next along the Z axis (or twist axis). Both the elastic U_L and the electrostatic U_E energy density contribute to the total free energy U in the cell. In this case we do not obtain explicit expressions for the distribution of the twist $\boldsymbol{c}$ and the tilt $\boldsymbol{q}$ angles as a function of z. Furthermore, these distributions depend on the applied voltage V, i.e. $\boldsymbol{c} = \boldsymbol{c}(z,V)$ and $\boldsymbol{q} = \boldsymbol{q}(z,V)$. In Figure 2.2 we represent the typical shapes of the nonlinear profiles for the twist $\boldsymbol{c}$ and the tilt $\boldsymbol{q}$ angles and for different voltages.
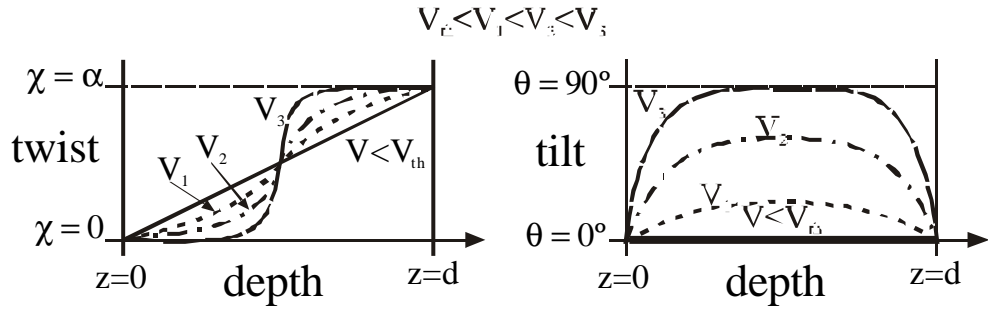

Figure 2.2. Typical profiles for the twist $\boldsymbol{c}$ and the tilt $\boldsymbol{q}$ angles and for different voltages.

Note that in Figure 2.2 the tilt angle q is zero at both ends as a result of the boundary conditions. Actually, the LC director exhibits a small pretilt angle Q, about 1-3 degrees, as commented in Section 1.2.1. The cell midpoint ($z=d/2$) tilt angle increases with the applied voltage and approaches 90 degrees at high applied voltages. For voltages high enough the twist angle c remains, in most of the cell, parallel to the director direction at both surfaces. Consequently, most of the twisting occurs within a thin layer around the cell midpoint. Note in Figure 2.2 that the twist angle c presents an odd symmetry around the cell midpoint, while the tilt angle q presents an even symmetry. We remember that the difference in the index of refraction Dn depends on the tilt angle q. Thus, the index of refraction varies along the cell depth z for varying voltages V, i.e. $Dn=Dn(z,V)$.
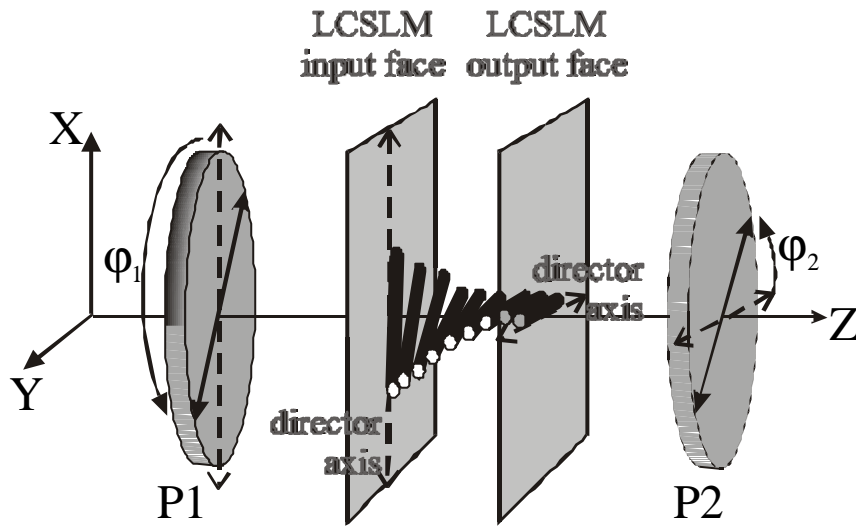

Figure 2.3. LCSLM inserted between two polarizers.

For most of the applications the TN-cell is inserted between two polarizers as we show in Figure 2.3. The cylinders in the LCSLM express the director distribution across the cell. j_1 and j_2 are the angles between the transmission axis of the input and the output polarizers with respect to the director axis in the input and in the output faces of the LCSLM respectively. The convention for the angles that we apply in this thesis is as follows. We consider that the observer is looking from the laser towards the detector, i.e. in the positive direction of the Z axis. The angles are taken to be positive when, for the observer, the sense from the director

axis to the transmission axis of the polarizer is clockwise. With this convention, the angles j_1 and j_2 represented in Figure 2.3 are positive.

In Section 1.2.2 we outlined the different methods to calculate the optical transmission of the cell. Either the Jones formalism or the more general 4x4 Berreman's method can be used. In the case of the field-on state it is not possible to determine an analytical expression for the Jones matrix of the LCSLM. Thus, the problem can only be addressed numerically. First, the values $c = c(z)$ and $q = q(z)$ are calculated for different values of applied voltage V. Second, the cell is divided in a series of uniaxial birefringent layers and the propagation of the beam of light is successively calculated through each of them. The second step has to be repeated for every new set (j_1, j_2) of orientations of the polarizers.

In the case of the field-off state it is possible to find an analytical formula for the intensity transmission of the LCSLM inserted between two polarizers. As we said in Section 1.2.2, Gooch and Tarry [Goo75] calculated the first analytical expression for the intensity transmission of the TN-cell. The Gooch and Tarry formula corresponds to the configuration with transmission axes of the polarizers parallel (or orthogonal) to the director axis at the input and at the output faces of the LCLSM respectively, i.e. $j_1 = j_2 = 0$ (or $\pi/2$). As it was mentioned in Section 1.2.3, these configurations (and their complementaries) are the ones that provide the best performance for display applications. This is true for the thick LCDs, which fulfill the Mauguin condition, i.e. $a << b$. Under this condition we take advantage of the polarization guiding effect. In the thin LCDs we will show, Section 2.1.2.2, that these particular configurations remain as interesting configurations even though the Mauguin condition is no longer fulfilled.

2.1.2 Reverse-engineering approach

The exact description reported in Section 2.1.1 needs the knowledge of the physical constants of the liquid crystal material and the fabrication parameters of the TN-cell (cell gap, range of applied voltage), that are not provided by the LCD manufacturers. Thus, we are forced to use a reverse-engineering approach and

design a simplified model for the twist c and the tilt q profiles that can provide a good estimation of the optical transmittance of the TN-cell. In this sense Lu and Saleh proposed a simplified model [Lu90] that has been a reference during the last years. An improved model was proposed by Coy *et al.* [Coy96] some years later. We recently proposed [PAPER A] a new simplified model for the TN-cell, based on these two previous models. The innovations we have introduced enable us for the first time to have a reverse-engineering approach model that not only provides qualitative results but also quantitative calculations of the optical transmission with a high degree of accuracy.

In this Section we develop this new model. We also show that the Lu and Saleh and the Coy *et al.* models can be derived as two particular cases of our more general proposal.

2.1.2.1 Model based on the voltage dependent edge effect

The goal is to approximate in a simple and intuitive way the nonlinear distributions of the twist c and the tilt q angles. The origin of these nonlinear profiles are the boundary conditions imposed by the anchoring of the LC molecules to the alignment layers. In Figure 2.2 we presented the realistic profiles of the twist c and the tilt q angles. We could see that the molecules in the vicinity of the alignment layers have a restricted freedom to move when a voltage is applied to the TN-cell. This edge effect must be taken into account by any model that pursuits an accurate description of the TN-cell.

In the model we propose in this thesis we take into account this edge effect by assuming that the TN-cell consists of three regions with a particular behavior:

(1) two edge layers, with a thickness d_1 each of them, where the LC molecules are unable to tilt and twist, thus acting as two wave plates.

(2) a central part, with a thickness d_2, which exhibits a homogeneous tilt and a linear twist with the cell depth.

The total thickness d of the cell is $d=2d_1+d_2$. In Figure 2.4 we illustrate the molecular director distribution with the cell depth z when the edge layers are introduced. This division of the TN-cell in three regions was first proposed by Coy *et al.* [Coy96].
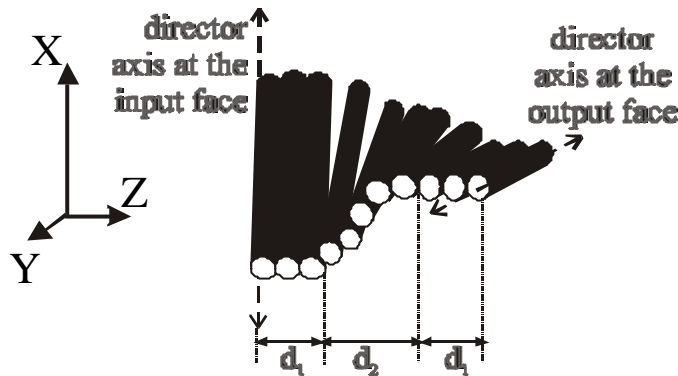

Figure 2.4. Diagram of the proposed model for the LC cell with the two edge layers of thickness d_1 and the central part of thickness d_2.

Another important feature can be extracted from Figure 2.2: the nonlinear profiles of the twist c and the tilt q angles vary with the applied voltage. This fact is included in the model by considering that the magnitude of the edge effect depends on the applied voltage, i.e. the thickness d_1 of the edge layers varies with the voltage. This voltage dependent edge effect is a novelty with respect to any previous model. The profiles for the twist c and the tilt q angles according to the model we propose are illustrated in Figure 2.5. The central part exhibits a twist c that depends linearly with the cell depth, i.e. $c = a(z-d_1)/d_2$ if $d_1 < z < d - d_1$, and the tilt angle q is constant with z in this region and varies with the applied voltage.
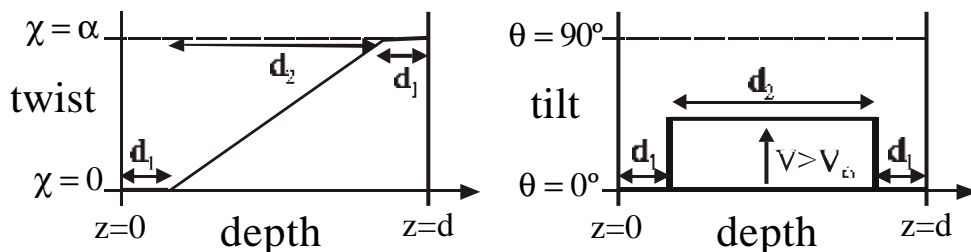

Figure 2.5. Profiles for the twist c and the tilt q angles as a function of the depth for different voltages. The thicknesses d_1 and d_2 vary with the voltage.

In the following we develop the corresponding birefringence parameters for the two regions in the TN-cell:

(1) Edge layers.- The birefringence $\boldsymbol{d}$ for each of the edge layers is given by

$$\boldsymbol{d}(V) = \boldsymbol{p}\, d_1(V)\, \boldsymbol{D} n_{max} / \boldsymbol{l} \qquad (2\text{-}9)$$

where $\boldsymbol{l}$ is the wavelength of the incident light. Additionally, the thickness d_1 varies with the voltage. $\boldsymbol{D} n_{max}$ is the difference between the extraordinary and the ordinary index, i.e. it is a maximum because the LC molecules are not tilted. As the director do not twist nor tilt the two edge layers can be represented as two wave plates, each one with a retardance $2\boldsymbol{d}$.

(2) Central part.- The twist $\boldsymbol{c}$ is a linear function of z, and the tilt angle $\boldsymbol{q}$ is homogeneous for all the LC molecules. Moreover, the tilt angle varies with the voltage. Therefore, the central part of the TN-cell can be described by a Jones matrix with the same formal expression as the Jones matrix presented in Eq. (2-5) but now the birefringence parameter varies with the voltage $\boldsymbol{b}(V)$. The birefringence $\boldsymbol{b}(V)$ is given by

$$\boldsymbol{b}(V) = \boldsymbol{p}\, d_2(V)\, \boldsymbol{D} n(V) / \boldsymbol{l} \qquad (2\text{-}10)$$

where both the index difference $\boldsymbol{D} n$ and the thickness d_2 depend on the voltage.

Hence, the total birefringence of the TN-cell is $\boldsymbol{d} + \boldsymbol{b} + \boldsymbol{d}$. The retardance generated between the extraordinary and the ordinary rays propagating across the TN-cell is twice this value, i.e. the total retardance is $2\boldsymbol{d} + 2\boldsymbol{b} + 2\boldsymbol{d}$, as commented in Section 1.2.1.

We want to add a quotation to the expression of the edge layers birefringence $\boldsymbol{d}(V) = \boldsymbol{p}\, d_1(V)\, \boldsymbol{D} n_{max} / \boldsymbol{l}$. Let us provide a more realistic image of the edge effect. Once again we take a look at Figure 2.2. The twist angle $\boldsymbol{c}$ remains approximately constant in the vicinity of the surfaces of the TN-cell, and the length of the region where it remains constant increases with the applied

voltage. However, we can see that the tilt angle q is not constant in the vicinity of the surfaces: actually, the highest the applied voltage the largest the variation in q Thus, we define as d_1' the thickness of the region in the vicinity of the surfaces where the twist angle c remains constant. Inside of this region the tilt angle q is not constant and, therefore, the index difference varies with z, i.e. $Dn(z,V)$. Thus, a more rigorous expression for the d birefringence is

$$d(V) = \frac{p}{l} \int_{z=0}^{z=d_1'(V)} Dn(z,V)dz = \frac{p}{l} \int_{z=d-d_1'(V)}^{z=d} Dn(z,V)dz \qquad (2\text{-}11)$$

where due to the symmetry of the TN-cell, the d birefringence value is the same in the two edge layers. A simplification can be made if we consider the mean value $\langle Dn(V) \rangle_{d_1'(V)}$ of the index difference in the edge layer, i.e.,

$$\langle Dn(V) \rangle_{d_1'(V)} = \frac{1}{d_1'(V)} \int_{z=0}^{z=d_1'(V)} Dn(z,V)dz \qquad (2\text{-}12)$$

Then Eq. (2-11) can be rewritten as

$$d(V) = p\, d_1'(V) \langle Dn(V) \rangle_{d_1'(V)} \big/ l \qquad (2\text{-}13)$$

In Figure 2.6 we show the profiles for the twist c and the tilt q angles according to the new details that we have considered in the voltage dependent edge effect model. We see that in the edge layers, the value for the tilt angle q is not zero.

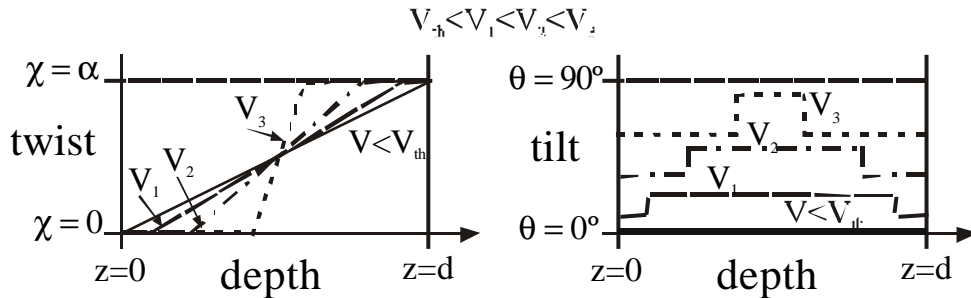**Figure 2.6.** Profiles for the twist c and the tilt q angles and for different voltages. The thicknesses d_1' and d_2' for the edge layers and the central part vary with the voltage.

Actually, Eq. (2-9) and Eq. (2-13) are different. However, we have no way to distinguish if the variation in the birefringence is caused either by a change in the thickness of the edge layer or by a change in the index difference. Thus, the value for $d(V)$ calculated with both expressions is the same. For the sake of simplicity, in [PAPER A] we have considered that the variation in $d(V)$ is simply due to a change in the thickness of the edge layer, leading to Eq. (2-9).

Our next step is to calculate the expression for the Jones matrix of the LCSLM according to the voltage dependent edge effect that we propose. We know that the edge layers can be described as two wave plates, each of them with a retardance $2d$. The extraordinary axis of these wave plates is oriented parallel to the LC director at the input and at the output surfaces respectively. The liquid crystal materials used to fill the LCSLMs have a positive dielectric anisotropy, $De = e_{/\!/} - e_\wedge > 0$. Thus, the extraordinary axis of the wave plates acts as the slow axis. The central part can be described with the same formal expression as the Jones matrix presented in Eq. (2-5) by simply replacing b by $b(V)$. The resultant matrix for the LCSLM, M'_{LCSLM}, is given by the following matrix product

$$M'_{LCSLM}(a,b,d) = \{R(-a) \cdot W_0(2d) \cdot R(+a)\} \cdot M_{LCSLM}(a,b) \cdot W_0(2d) \quad (2\text{-}14)$$

Here $W_0(2d)$ is the Jones matrix for a wave plate with a retardance $2d$, i.e.,

$$W_0(2d) = \begin{pmatrix} exp(-id) & 0 \\ 0 & exp(id) \end{pmatrix} \quad (2\text{-}15)$$

The matrix $M'_{LCSLM}(a,b,d)$ can be simplified as

$$M'_{LCSLM}(a,b,d) = exp(-i(b+2d))R(-a)\begin{pmatrix} X'-iY' & Z \\ -Z & X'+iY' \end{pmatrix} \quad (2\text{-}16)$$

where we define new parameters X' and Y' as

$$X' = X\cos 2d - Y\sin 2d \quad (2\text{-}17a)$$

$$Y' = X\sin 2d + Y\cos 2d \quad (2\text{-}17b)$$

Note that the parameter Z does not depend on the birefringence of the edge layers while both X' and Y' are affected by the existence of the edge layers. It is important to remark that the LCSLM is a non-absorbing device. Then, the matrix $M'_{LCSLM}(\boldsymbol{a},\boldsymbol{b},\boldsymbol{d})$ is unitary, i.e. its determinant is equal to one. From this property we find a useful relation that links the three parameters $X'^2 + Y'^2 + Z^2 = 1$. Fernández-Pousa *et al.* [Fer00] provide some general relations based on symmetry based arguments between the matrix elements of the Jones matrix for the TN-LCSLM.

The expression $M'_{LCSLM}(\boldsymbol{a},\boldsymbol{b},\boldsymbol{d})$ in Eq. (2-16) is the one proposed and verified in [PAPER A] to describe the TN-cell behavior. From a mathematical point of view, the model we propose has two degrees of freedom for each voltage value. They are the birefringence of the two edge layers $\boldsymbol{d} = \boldsymbol{d}(V)$, and the birefringence of the central part $\boldsymbol{b} = \boldsymbol{b}(V)$. The LCSLM is totally described when we know the values for these two parameters for each applied voltage value.

Once we have an analytical expression for the Jones matrix of the LCSLM we can calculate the intensity transmission and the phase modulation when the LCSLM is inserted between polarizing devices. Here we show the calculation done in [PAPER A] for the LCSLM inserted between two polarizers. Note that in this thesis the convention for the angles is different with respect to [PAPER A]. As illustrated in Figure 2.3, $\boldsymbol{j}_1$ and $\boldsymbol{j}_2$ are the angles of the transmission axes of the polarizers with respect to the director axis at the input and the output face of the LCSLM respectively. The electric field vector $\vec{E}_{OUT}$ at the output of this system is given by the following matrix product

$$\vec{E}_{OUT} = P_X\, R(\boldsymbol{a}+\boldsymbol{j}_2)\, M'_{LCSLM}(\boldsymbol{a},\boldsymbol{b},\boldsymbol{d})\begin{pmatrix}\cos\boldsymbol{j}_1\\ sin\boldsymbol{j}_1\end{pmatrix} \qquad (2\text{-}18)$$

where P_X is the Jones matrix of a linear polarizer with its transmission axis oriented parallel to the X-coordinate axis, let us say:

$$P_X = \begin{pmatrix} 1 & 0 \\ 0 & 0 \end{pmatrix} \tag{2-19}$$

The output amplitude vector $\vec{E}_{OUT}$ is expressed in the coordinate system formed by the axes of the output polarizer. The resultant output vector $\vec{E}_{OUT}$ transmitted by the system is given by

$$\vec{E}_{OUT} = \exp(-i(\boldsymbol{b}+2\boldsymbol{d}))\begin{pmatrix} X'\cos(\boldsymbol{j}_1 - \boldsymbol{j}_2) + Z\sin(\boldsymbol{j}_1 - \boldsymbol{j}_2) - iY'\cos(\boldsymbol{j}_1 + \boldsymbol{j}_2) \\ 0 \end{pmatrix} \tag{2-20}$$

The intensity transmission T of the system is calculated as the hermitic scalar product of the output electric field vector $\vec{E}_{OUT}$

$$T = \vec{E}_{OUT}^\dagger \cdot \vec{E}_{OUT} \tag{2-21}$$

where $\vec{E}_{OUT}^\dagger$ is the hermitic conjugate of the vector $\vec{E}_{OUT}$. From Eq. (2-20) it is trivial to see that the complex amplitude component E_t transmitted by the analyzer is given by,

$$E_t = \exp(-i(\boldsymbol{b}+2\boldsymbol{d}))[X'\cos(\boldsymbol{j}_1 - \boldsymbol{j}_2) + Z\sin(\boldsymbol{j}_1 - \boldsymbol{j}_2) - iY'\cos(\boldsymbol{j}_1 + \boldsymbol{j}_2)] \tag{2-22}$$

The phase value, or phase-shift $\boldsymbol{y}$, for the transmitted component E_t is given by

$$\boldsymbol{y} = atan\left(\frac{Im[E_t]}{Re[E_t]}\right) \tag{2-23}$$

where Re[] and Im[] express the real and the imaginary part respectively, and *atan()* is the inverse tangent function. Thus, the intensity transmission T is

$$T = [X'\cos(\boldsymbol{j}_1 - \boldsymbol{j}_2) + Z\sin(\boldsymbol{j}_1 - \boldsymbol{j}_2)]^2 + [Y'\cos(\boldsymbol{j}_1 + \boldsymbol{j}_2)]^2 \tag{2-24}$$

and the resultant phase-shift $\boldsymbol{y}$ is given by

$$\boldsymbol{y} = -\boldsymbol{b} - 2\boldsymbol{d} - atan\left(\frac{Y'\cos(\boldsymbol{j}_1 + \boldsymbol{j}_2)}{X'\cos(\boldsymbol{j}_1 - \boldsymbol{j}_2) + Z\sin(\boldsymbol{j}_1 - \boldsymbol{j}_2)}\right) \tag{2-25}$$

To calculate the intensity transmission and the phase-shift for a particular LCSLM, we need to know some magnitudes in Eq. (2-24) and (2-25). We group

the unknowns in two different categories: the voltage independent unknowns and the voltage dependent unknowns.

There are two voltage independent unknowns: the orientation of the molecular director at the input face Y_D, and the total twist angle a. To determine the values for the angles j_1 and j_2 we must find the orientation of the molecular director at the input face Y_D and at the output face Y_{DOUT} with respect to the laboratory coordinate system. Actually, Y_{DOUT} can be found from the values of Y_D and a as $Y_{DOUT} = Y_D + a$. The value for the twist angle a is also required to calculate X', Y' and Z. In Section 2.2.2 we show how to calculate Y_D and a according to the technique proposed by Soutar and Lu [Sou94b]. The two voltage dependent unknowns are the birefringences $b(V)$ and $d(V)$. In Section 2.2.4 we describe the experimental technique proposed in [PAPER A] for calculating these two parameters as a function of applied voltage. The values calculated for $d(V)$ characterize the voltage dependent edge effect existing in the LCSLM.

2.1.2.2 Previous models as particular cases

In this Section we will show how the previous simplified models, the one proposed by Lu and Saleh [Lu90] and the one proposed by Coy *et al.* [Coy96], can be derived as particular cases of the general model we have developed.

We illustrate that the model of Lu and Saleh corresponds to the case in which no edge effect exists, i.e. $d = 0$. As Lu and Saleh comment [Lu90,Lu91a] they approximated the nonlinear distributions of the twist c and the tilt q angles considering the following approximations:

(1) Since the tilt angle $q = q(z,V)$ is a smoothly varying function with even symmetry around the midpoint ($z = d/2$) it is approximated by its mean value.

(2) Since the twist angle $c = c(z,V)$ is a smoothly varying function with odd symmetry around the midpoint $(z = d/2)$, it is approximated by a linear function of z, $c = a\,z/d$.

In Figure 2.7 we represent the twist c and the tilt q profiles according to these two approximations. In the model of Lu and Saleh there is no edge effect, therefore $d = 0$. The whole LC cell is behaving as the central part described in the voltage dependent edge effect model. The previous Jones matrix in Eq. (2-16) reduces to a Jones matrix with the same formal expression as Eq. (2-5) with the substitution of b by $b(V)$.
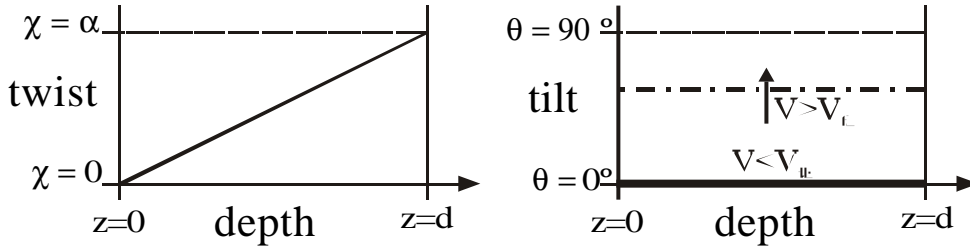

Figure 2.7. Profiles for the twist c and the tilt q angles for different voltages according to the Lu and Saleh model.

The Lu and Saleh model was not able to give accurate quantitative results of the performance of the LC cell. This led Coy *et al.* to modify the Lu and Saleh model [Coy96]. Coy *et al.* considered that the molecules close to the surfaces do not tilt nor twist. Consequently, these molecules act as two wave plates located at these surfaces. Coy *et al.* considered the thickness of these two wave plates constant with the applied voltage. Thus, their proposal can be derived from the general model in Eq. (2-16) simply by considering $d = constant$. In Figure 2.8 we show the corresponding profiles for the twist c and the tilt q angles.

Actually, the nonlinear profiles reported by the exact description (Figure 2.2) vary significantly with the applied voltage. Thus, as we proof in [PAPER A], even though the Coy *et al.* model provides better results than the Lu and Saleh model, it is still far from giving an accurate calculation of the optical transmittance for the TN-cell.
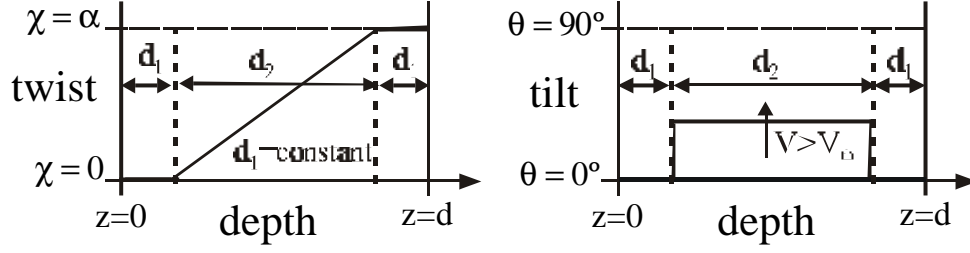
Figure 2.8. Profiles for the twist *c* and the tilt *q* angles for different voltages according to the Coy *et al.* model. The thicknesses d_1 and d_2 are constant.

In the following, using Eq. (2-24) and (2-25) we show some theoretical simulations for the intensity transmission and the phase-shift. We plot the simulated values versus the *b* birefringence. We consider a range of *500* degrees for the *b* birefringence. This value, *500* degrees, can be considered a typical value for the maximum *b* birefringence in the case of a thick LCSLM. In the thin LCSLMs the maximum *b* birefringence is about *200* degrees or lower, depending on the wavelength of the incident light as well. We know that the *b* birefringence is a function of the applied voltage, i.e. *b* = *b(V)*. The *b* birrefringence decreases monotonously with the increase in the applied voltage.

We compare the simulations obtained under two different situations: on one hand, considering the existence of edge layers and, on the other hand, omitting the edge layers. We have calculated the curves for two different values of the *d* birefringence for the edge layers: *d* = *10* degrees and *d* = *20* degrees. We concentrate our attention in some specific configurations of the polarizers that are especially interesting for our purposes. In the simulations we consider that the total twist angle *a* for the LCSLM is equal to 90 degrees.

First, we consider the typical configurations used in display applications. As we have commented, they are *j*$_1$ = *j*$_2$ = *0*^{o}, and *j*$_1$ = *j*$_2$ = *90*^{o}. Actually, the complementary configurations, i.e. *j*$_1$ = *0*^{o}, *j*$_2$ = *90*^{o} and *j*$_1$ = *90*^{o}, *j*$_2$ = *0*^{o}, are equally good for display applications. In Figure 2.9 we plot the results for the configuration *j*$_1$ = *j*$_2$ = *90*^{o}. The intensity transmission curves, Figure 2.9(a), and the phase-shift curves, Figure 2.9(b), are identical for the three cases considered, *d* = *0* deg., *d* = *10* deg. and *d* = *20* deg. Thus, this configuration is not sensitive to

the existence of the edge layers. A display configuration should provide a high contrast between the dark (minimum intensity transmission) and the bright (maximum intensity transmission) states. We can see that if we use the b range between *0* deg. and *155* deg. we achieve the maximum possible contrast between the dark and the bright states. For values of b higher than *155* deg., the intensity transmission follows an attenuating oscillatory behaviour that gradually approaches to the maximum transmission value: the LCSLM is under the Mauguin regime condition, i.e. $\alpha \ll b$. In the complementary configuration, $j_1 = 0^o$, $j_2 = 90^o$, the dark and the bright states are interchanged: $b = 0$ deg. is the bright state, and $b > 155$ deg. is the dark state.

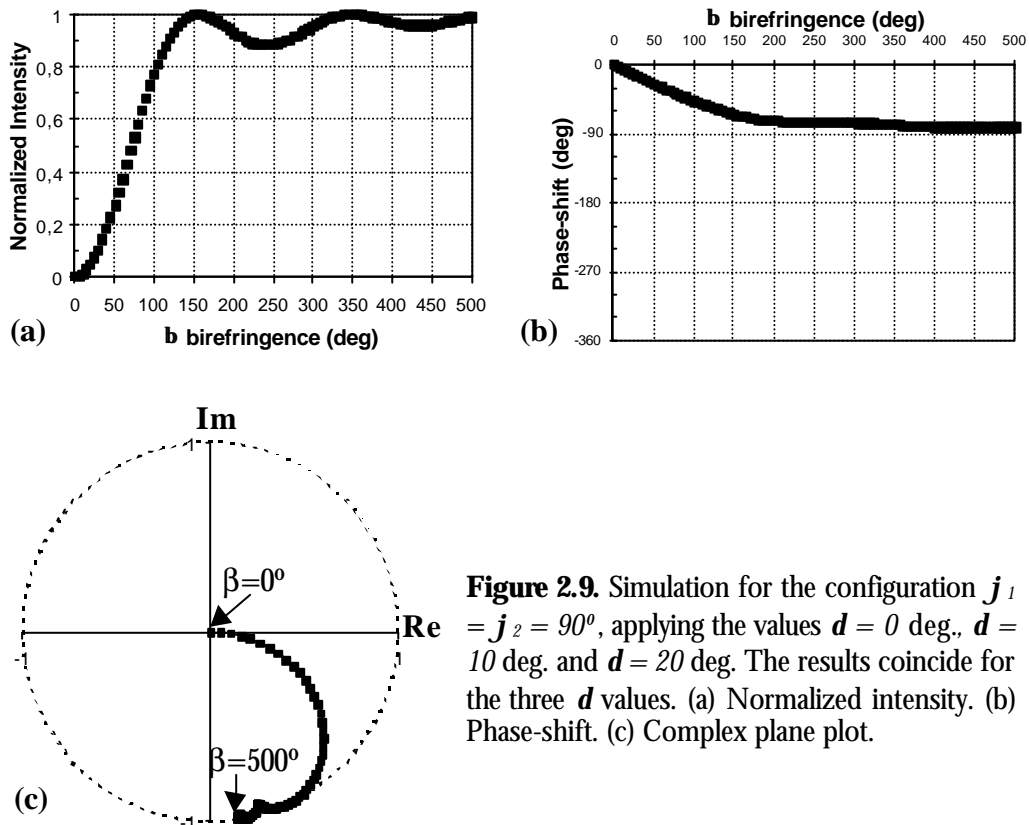**Figure 2.9.** Simulation for the configuration $j_1 = j_2 = 90^o$, applying the values $d = 0$ deg., $d = 10$ deg. and $d = 20$ deg. The results coincide for the three d values. (a) Normalized intensity. (b) Phase-shift. (c) Complex plane plot.

The thick LCSLMs benefit from the Mauguin regime to produce a good intensity contrast in an easy way. The polarizers have to be oriented in the configurations $j_1 = j_2 = 0^o$, $j_1 = j_2 = 90^o$, or the complementaries. In the next explanation let us consider the configuration $j_1 = j_2 = 90^o$, i.e. both polarizers are orthogonally oriented to each other. When a high voltage is applied b is equal to *0*

deg.: for $b=0$ deg. the director is parallel to the twist axis and the light propagating along the twist axis does not change its polarization state. Hence, the incident linearly polarized light is blocked by the orthogonally oriented output polarizer: the dark state is generated. When no voltage is applied the LCSLM fulfills the Mauguin regime, i.e. $\alpha<<b$, and the polarization guiding effect takes place. The incident linearly polarized light follows the twist of the director across the cell. Thus, the output polarizer transmits all the light: the bright state is generated. As long as $\alpha<<b$, this excellent intensity contrast is not sensitive to errors in the resultant thickness of the liquid crystal layer during the fabrication process. Moreover, as long as $\alpha<<b$, the contrast is not sensitive to the wavelength of the incident light (so we can use white light sources as it is the case in display applications). The main drawback of the thick LCSLMs is their slow response to the change in the applied voltage. The time response is proportional to the square of the thickness of the LC-cell. The higher resolution, i.e. the larger number of pixel elements to be addressed, in the newer generations of displays requires a faster time response to the electrical signal applied. One of the solutions has been to produce LCSLMs with a thickness reduced to the minimum length possible while keeping a good contrast in display applications: the condition is that the resultant b for the field-off state has to be about *155* deg. Thus, the thin LCSLMs does not benefit from the large margin of tolerance given by the Mauguin regime condition. This makes the fabrication process and the field-on operation much more critical.

In display applications the phase-shift modulation of the light is unimportant because we work with incoherent light and the physical magnitude of interest is the intensity. In other applications where we use coherent light the physical magnitude of interest is the complex amplitude, hence, the phase-shift modulation has to be taken into consideration. If we look at the phase-shift curve in Figure 2.9(b) we observe that the range of phase-shift is less than *90º*. Thus, if working in a range of b between *0* deg. and less than *155* deg. we obtain a high contrast with a reasonable low phase-shift coupling. This configuration, $j_1 = j_2 = 90º$, has been widely used when amplitude-only modulation was required. In

Figure 2.9(c) we show the representation in the complex plane for the complex amplitude transmission where we appreciate the coupling between amplitude and phase-shift modulations.
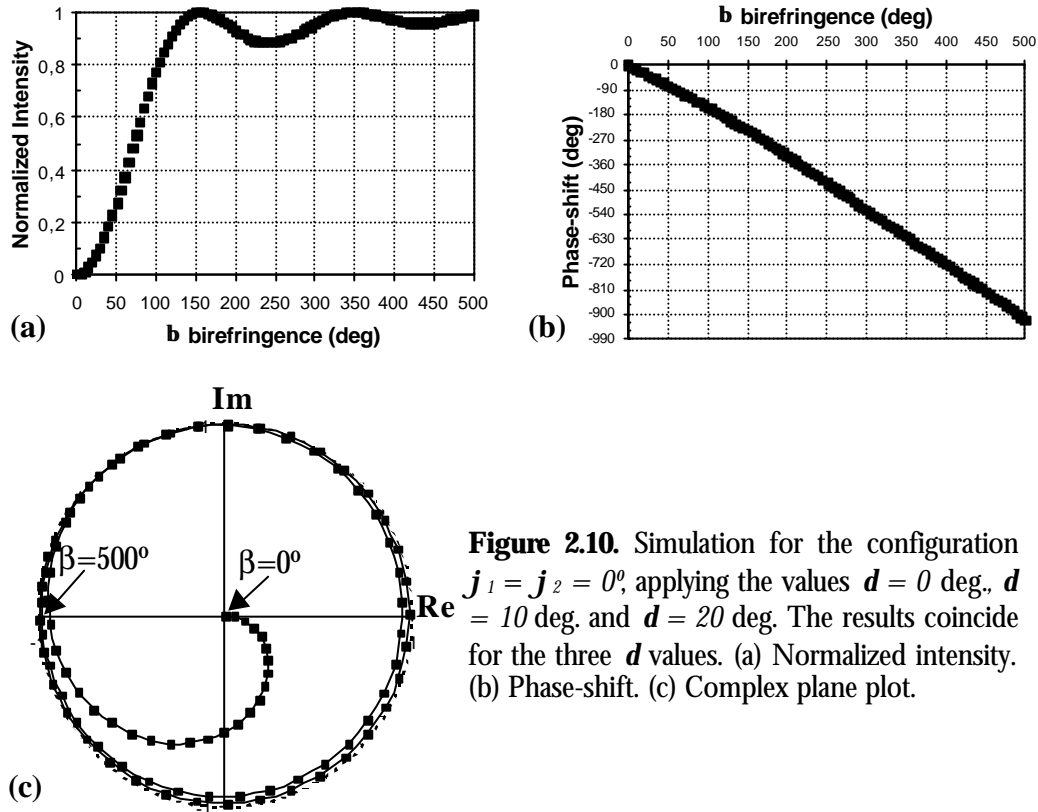

(a)

(b)

(c)

Figure 2.10. Simulation for the configuration $j_1 = j_2 = 0^o$, applying the values $d = 0$ deg., $d = 10$ deg. and $d = 20$ deg. The results coincide for the three d values. (a) Normalized intensity. (b) Phase-shift. (c) Complex plane plot.

In Figure 2.10 we present the results for the configuration $j_1 = j_2 = 0^o$. As in the previous configuration the intensity transmission curves and the phase-shift curves are identical for the three cases considered, $d = 0$ deg., $d = 10$ deg. and $d = 20$ deg. Thus, this configuration is not sensitive to the existence of the edge layers. We can see that the intensity transmission curve is identical to the one presented in Figure 2.9(a). Thus, the configuration $j_1 = j_2 = 0^o$ and its complementary $j_1 = 0, j_2 = 90^o$ are also appropriate configurations for display applications. In Figure 2.10(b) we can see that the phase-shift modulation has a monotonous behaviour and a very large range of variation. If we limit the range of operation to b values higher than *155* deg., we can obtain a large phase-shift modulation with a very low coupling of intensity transmission modulation. The configuration $j_1 = j_2 = 0^o$, using the range $b > 155$ deg., has been the typical one used when phase-only

modulation was required. Obviously, in the thin LCSLMs this configuration can not be obtained because the birefringence does not get so high values. In Figure 2.10(c), we show the representation of the complex amplitude transmission. We can see that, excluding the low b birefringence points, the curve is practically overlapped with the unit circle.

Even though we do not plot the results in this thesis, we want to remark that in the simulations for the two complementary configurations, i.e. $j_1 = 0^o$, $j_2 = 90^o$ and $j_1 = 90^o$, $j_2 = 0^o$, once again the edge effect is not apparent.
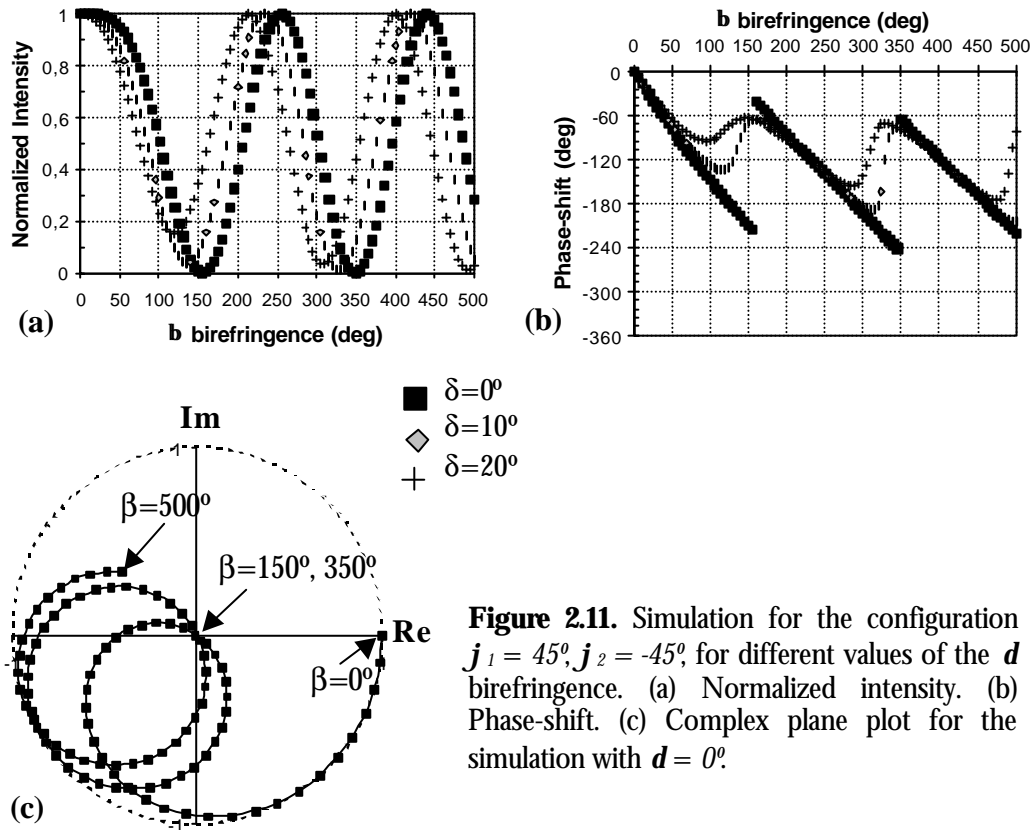
Figure 2.11. Simulation for the configuration $j_1 = 45^o$, $j_2 = -45^o$, for different values of the d birefringence. (a) Normalized intensity. (b) Phase-shift. (c) Complex plane plot for the simulation with $d = 0^o$.

In Figure 2.11 we show the results for the configuration $j_1 = 45^o$, $j_2 = -45^o$. In this case we see that we obtain clearly different intensity and phase-shift curves for the three values considered for the d birefringence ($d = 0$ deg., $d = 10$ deg. and $d = 20$ deg.). Thus, this is an interesting configuration in order to verify the existence of the edge effect and, therefore, to validate the model we propose. If we look at the intensity transmission, Figure 2.11(a), we can see that for $d = 0^o$

the curve attains maximum values equal to 1 and minimum values equal to 0. For $d = 10$ deg. and $d = 20$ deg., the intensity curve is shifted with respect to the curve corresponding to $d = 0$ deg. Moreover, the minimum intensity is not zero. In the phase-shift curves, Figure 2.11(b), we also observe different behaviours. For $d = 0$ deg. the phase-shift is a discontinuous curve with a monotonous behaviour in each of its sections. For $d = 10$ deg. and $d = 20$ deg., the phase-shift curve is continuous but with a non-monotonous behaviour. We note that the phase jumps in the curve for $d = 0$ deg. are located at the b values where the intensity transmission is zero. In Figure 2.11(c) we have plotted in the complex plane the complex amplitude transmission for $d = 0$ deg. We see that this is a continuous curve with a highly coupled amplitude and phase-shift modulations. In general, for arbitrary values of j_1 and j_2 the amplitude and the phase-shift are highly coupled.

We have seen in Figure 2.9 and in Figure 2.10 two configurations not sensitive to the edge effect. In fact, these two configurations and their complementary are the only ones which are not sensitive to the edge effect. In general, the edge effect has an influence on the optical transmission as in the case shown in Figure 2.11.

2.2 Characterization of the LCSLM

In this Section we introduce with further detail the different methods mentioned in [PAPER A] and [PAPER B] which are required to characterize the LCSLM. First of all we show in Section 2.2.1 the specifications of our LCSLM and the video projector from which it has been extracted. In Section 2.2.2 the method we follow to obtain the voltage independent magnitudes of the LCSLM is explained. The experimental set-ups used for measuring the intensity transmission and the phase-shift as a function of the gray level are presented in Section 2.2.3. Finally, the technique we propose in [PAPER A] to characterize the edge effects in the LCSLM is introduced in Section 2.2.4, and in Section 2.2.5 some results are presented in which we verify the validity of the proposed model to explain the

behavior of the LCSLM. The experimental results are in excellent agreement with the numerical results obtained with the proposed method.

2.2.1 Description of the LCSLM and the video projector

In general, due to its low cost and large availability the LCSLMs used in research are the LCD panels extracted from commercial LCD-video projectors. These panels are designed for an optimum performance in display applications, but with the proper adaptations they can also be used in optical information processing, in programmable diffractive optics, and in adaptive optics. In this work the LCSLMs we use have been extracted from a Sony Model VPL-V500 video projector. This is a projection system for color images in VGA format. It consists of three main components: (a) the source of light (a white light lamp), (b) the electronics for the control of the video projector, and (c) an optical system formed by three LCD panels with a recombining prism, lenses, dichroic mirrors, and a projection objective. In Figure 2.12 the scheme for this video projector is presented.
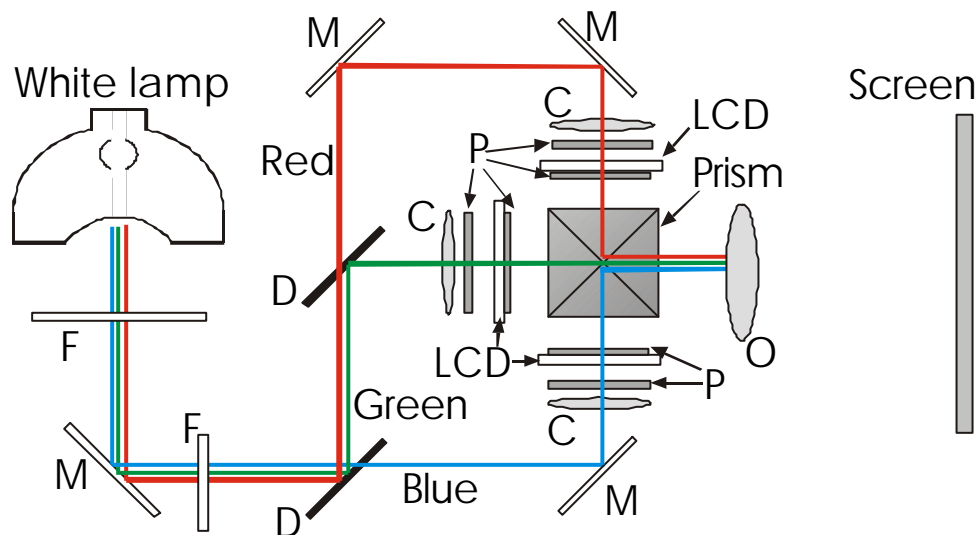

Figure 2.12. Schematic diagram of the optical elements of the video projector. F: eye-fly lens, M: mirror, D: dichroic beam splitter, C: condenser lens, P: polarizer, O: objective lens, LCD: liquid crystal display.

As we can see in Figure 2.12, the original beam of light coming from the white lamp (250 W metallic halur lamp) is separated in three different beams (red,

green, and blue) by means of two dichroic mirrors. Each beam impinges onto a LCD panel. The electronics separates the three colour components (red, green and blue) of the VGA image that we want to project and send the signals to the associated panels. Once the light beams have been modulated, they are recombined by means of a prism to produce the desired image in color. The objective projects the final image onto a screen.
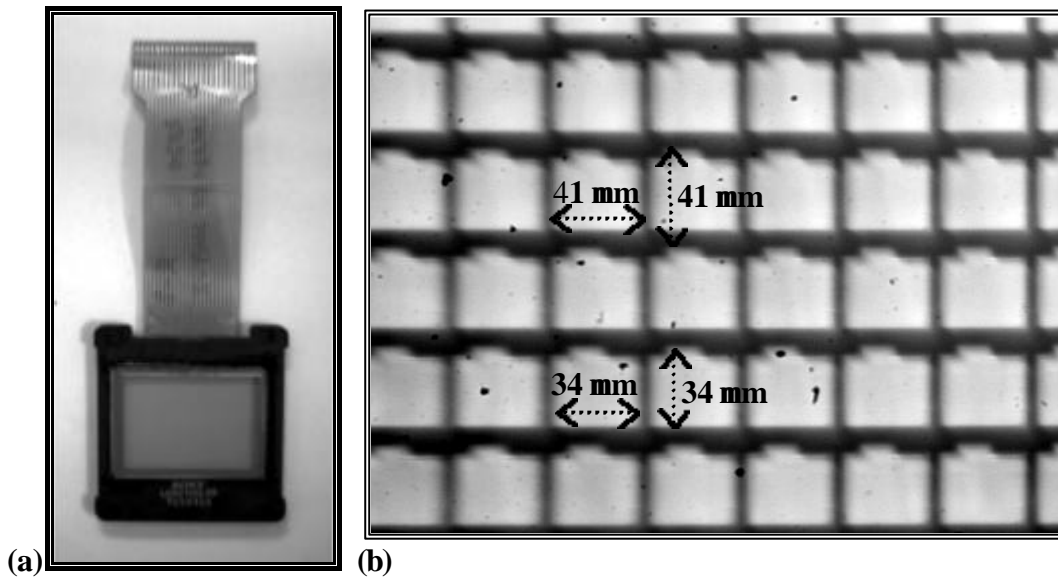

Figure 2.13. (a) LCSLM Sony Model LCX012BL, we can see the panel and the flexible printed circuit (FPC), (b) Magnified image of the pixelated structure of the LCSLM. The dark areas correspond to the electrode wires and to the thin film transistor (TFT) and the capacitor for each pixel.

The LCD panels we use are Sony Model LCX012BL. In Figure 2.13 a picture of this LCSLM is shown. The Sony Model LCX012BL is a 3.3 cm diagonal active matrix TFT-LCD panel addressed by polycrystalline silicon super thin film transistors (TFT) with built-in peripheral driving circuit. The TFT active matrix technology provides pixel by pixel control of the display. The small rectangles in the upper side of each pixel, Figure 2.13(b), are the TFTs and capacitors. The pixels are square with a pixel center to center separation of 41 μm and with a pixel width of 34 μm. The number of pixels is 311696 (644 x 484 pixels). The video projector accepts the computer requirements of VGA platform (640 x 480 pixels). An additional graphic card has been inserted in the personal computer to send VGA images to the video projector. The VGA image consists of

three different channels (red, green and blue) in order to produce full color images. In each channel the image is visualized with 8 bits, that is $2^8 = 256$ gray scale levels (GSL). The voltage applied to each pixel is a magnitude related with the gray level sent in the image to the corresponding channel in which the LCD is connected. We note that the electronics for the Sony VPL-V500 video projector produces a decrease in the voltage when the GSL is increased.

In order to use the LCD panels as LCSLMs in an optical set-up we had to extract them from the video projector. The original connection of the LCD to the electronics of the video projector is very short, so we had to connect the LCD through a longer cable especially designed for this purpose. The LCD has a sheet polarizer attached on one side. This sheet polarizer and the white lamp are both removed. We note that the video projector turns off automatically when there is no lamp connected. A connection in the printed circuit board (PCB) has been added to enable the video projector working with no lamp. The image in the video projector is controlled through two commands, brightness (B) and contrast (C), which modify respectively the voltage offset and the voltage gain of the GSLs applied. The values of these controls range from 0 to 100. We have found that an increase in the brightness produces a decrease in the voltage offset, and an increase in the contrast produces an increase in the absolute value of the voltage gain. Considering a linear relation between the voltage V and the GSL the effect of the brightness B and the contrast C values can be expressed as

$$V = (V_{max} - a \cdot B) - b \cdot C \cdot GSL \qquad (2\text{-}26)$$

where V_{max} is the maximum voltage that can be addressed to the LCSLM, and a and b are positive constants.

2.2.2 Determination of the director orientation and the twist angle

In Section 2.1.2.1 we established that different magnitudes have to be calculated in order to use Eq. (2-24) and (2-25). In this Section we expose the method to find the voltage independent magnitudes, $\mathbf{Y}_D$ and $\mathbf{a}$, according to the method proposed by Soutar and Lu [Sou94b]. Since the LCSLMs have been

developed under proprietary conditions, little or nothing may be known about any particular LC cell that we desire to model. This is the reason why Soutar and Lu mention in their paper that *"determination of the unknown parameters requires a reverse-engineering procedure"*. In [PAPER A] and [PAPER B] this technique was summarized. Here, we will give more details.

In these experiments the LCSLM is inserted between the polarizer and the analyzer. In Figure 2.14 we show a general scheme for this experiment with the different angles to be considered. We can measure the angles z_1 and z_2 of the transmission axes of the polarizers with respect to the laboratory vertical. Then the angles j_1 and j_2 that appear in Eq. (2-24) and (2-25), defined with respect to the director in the input and in the output face of the LCSLM respectively, can be related to z_1 and z_2 as follows

$$z_1 = j_1 + Y_D \tag{2-27a}$$

$$z_2 = j_2 + a + Y_D \tag{2-27b}$$

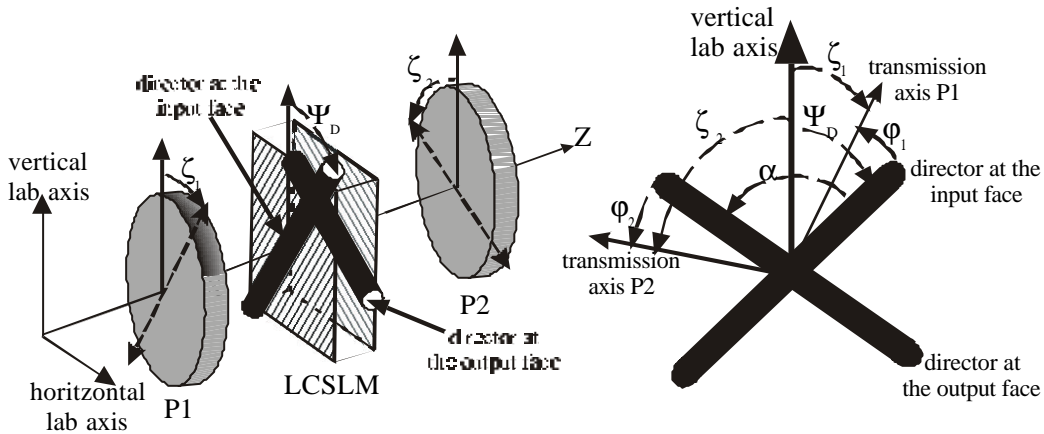where the unknown magnitudes Y_D and a appear.

Figure 2.14. Scheme for the angles notation that we use in the experiment in order to determine the voltage independent magnitudes.

We introduce in Eq. (2-24) the changes of variables reported in Eq. (2-27a) and (2-27b). The LC cell is considered in the field-off state ($d = 0$). Therefore, the transmission is given by

$$T = \left[X\,cos(\textbf{\textit{z}}_1 - \textbf{\textit{z}}_2 + \textbf{\textit{a}}) + Z\,sin(\textbf{\textit{z}}_1 - \textbf{\textit{z}}_2 + \textbf{\textit{a}}) \right]^2 + \left[Y\,cos(\textbf{\textit{z}}_1 + \textbf{\textit{z}}_2 - \textbf{\textit{a}} - 2\textbf{\textit{Y}}_D) \right]^2 \quad (2\text{-}28)$$

Apart from $\textbf{\textit{Y}}_D$ and $\textbf{\textit{a}}$, we have a further unknown: the birefringence $\textbf{\textit{b}}$ that appears together with $\textbf{\textit{a}}$ in the expressions for X, Y and Z (Eq. (2-8)). In the field-off state the birefringence is maximum so we can write $\textbf{\textit{b}}_{max}$. For simplicity, we consider two specific cases, crossed ($\textbf{\textit{z}}_1 = \textbf{\textit{z}}_2 + \pi/2$) and parallel ($\textbf{\textit{z}}_1 = \textbf{\textit{z}}_2$) polarizers. The intensity transmission of the system in these two cases is given by

$$T_{crossed} = N \left[\left[-cos\,\textbf{\textit{g}}\,sen\,\textbf{\textit{a}} + \frac{\textbf{\textit{a}}}{\textbf{\textit{g}}}\,sen\,\textbf{\textit{g}}\,cos\,\textbf{\textit{a}} \right]^2 + \left[\frac{\textbf{\textit{b}}}{\textbf{\textit{g}}}\,sen\,\textbf{\textit{g}}\,sen(2\textbf{\textit{z}}_1 - \textbf{\textit{a}} - 2\textbf{\textit{Y}}_D) \right]^2 \right] \quad (2\text{-}29\text{a})$$

$$T_{parallel} = N \left[\left[cos\,\textbf{\textit{g}}\,cos\,\textbf{\textit{a}} + \frac{\textbf{\textit{a}}}{\textbf{\textit{g}}}\,sen\,\textbf{\textit{g}}\,sen\,\textbf{\textit{a}} \right]^2 + \left[\frac{\textbf{\textit{b}}}{\textbf{\textit{g}}}\,sen\,\textbf{\textit{g}}\,cos(2\textbf{\textit{z}}_1 - \textbf{\textit{a}} - 2\textbf{\textit{Y}}_D) \right]^2 \right] \quad (2\text{-}29\text{b})$$

The common factor N accounts for light losses due to reflections in the interfaces and absorption in the polarizers. Thus, there are 4 unknowns (N, $\textbf{\textit{a}}$, $\textbf{\textit{b}}$, $\textbf{\textit{Y}}_D$).

We proceed with intensity measurements with crossed and parallel polarizers as a function of the polarizer angle $\textbf{\textit{z}}_1$. The four unknowns can be determined through a nonlinear curve fitting procedure using the theoretical expressions (2-29a) and (2-29b). According to Davis *et al.* [Dav99a] a unique determination of the values for the four unknowns is not possible if the measurements are obtained with only one wavelength. The reason is that we have four unknowns and only two constraints. In order to reduce the degrees of freedom in the fitting and to eliminate ambiguities they proposed to measure with different wavelengths. Particularly we have used the unexpanded beams for four different wavelengths: 633 nm from a He-Ne laser and the 514, 488 and 458 nm from an Ar$^+$ laser. The angles $\textbf{\textit{Y}}_D$ and $\textbf{\textit{a}}$ are wavelength independent, the birefringence $\textbf{\textit{b}}_{max}$ is obviously wavelength dependent. The normalization factor N is also wavelength dependent because we use dichroic sheet polarizers. In Figure 2.15. we show the dependence of the logarithm of the intensity transmission on the wavelength for the specific polarizers we use: dichroic polymer (DP) with the coating Vis-1 designed for the visible, fabricated by Meadowlark Optics.
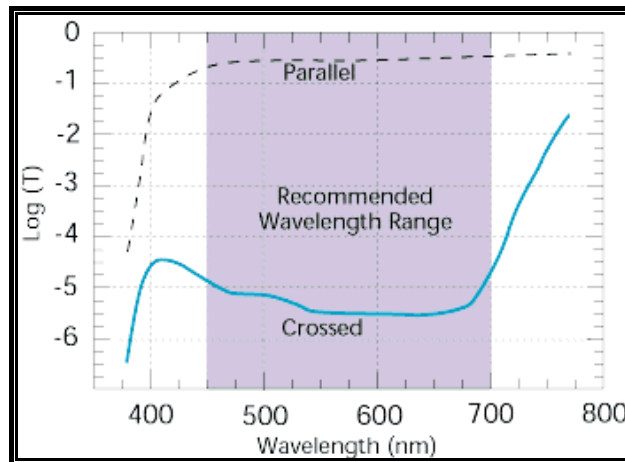
Figure 2.15. Dichroic polymer (DP) polarizer, of Meadowlark Optics, with the coating Vis-1 for the visible. Characteristic intensity transmission curves (logarithmic scale) for the transmission axis (parallel curve) and for the extinction axis (crossed curve) as a function of the wavelength.
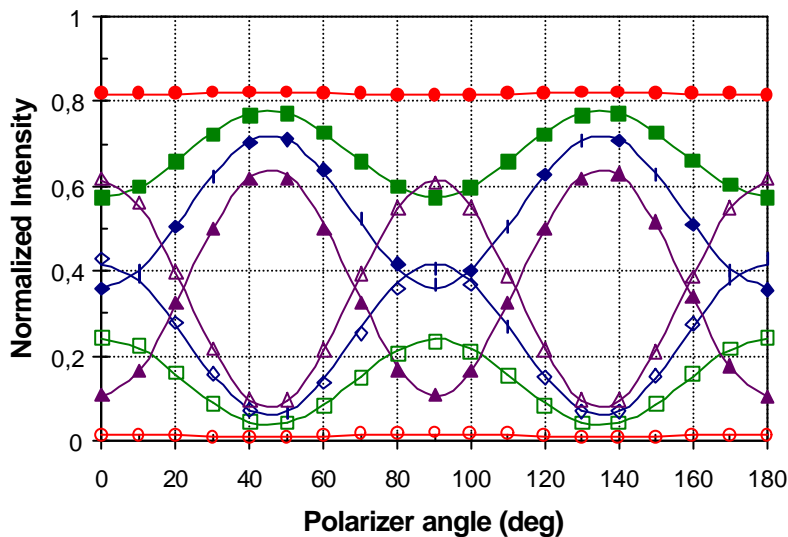

Figure 2.16. Crossed (filled symbols) and parallel (empty symbols) polarizers transmissions measured in the field-off state. The lines correspond to the fitting of the experimental data for the four wavelengths: 633 nm (circle), 514 nm (square), 488 nm (diamond), and 458 nm (triangle).

Using the Solver curve fitting routine in Microsoft Excel, we determine the set of values for the four unknowns that provide the best fit between the experimental measurements and the theoretical expressions. We have used this method with different LCSLMs (more than 9 units). In Figure 2.16 we plot the experimental curve and the theoretical fit obtained with one LCSLM Sony model LCX012BL for the four wavelengths. The intensity values in Figure 2.16 are

normalized by the total intensity at the output of the second polarizer. All the experimental results that we present along this thesis have been obtained using this particular LCSLM. This unit has also been employed in most of the papers of this thesis. We can visually perceive that the fitting is excellent for all the wavelengths either for crossed or for parallel polarizers.

The result we obtain depends neither on the sign of the twist angle $\boldsymbol{a}$, nor on the two possible values of the molecular director orientation in the input face $\boldsymbol{Y}_D$ or $\boldsymbol{Y}_D + \boldsymbol{p}/2$. Two further experiments need to be done in order to solve these two ambiguities in Eq. (2-29a) and (2-29b). The first ambiguity can be solved using a configuration of the polarizers that provides an intensity transmission dependent on the sign of the twist angle $\boldsymbol{a}$. One such configuration is for example, input polarizer remains parallel to the laboratory vertical ($\boldsymbol{z}_l = 0$) and the intensity measurements are taken at different angles $\boldsymbol{z}_2$ of the output polarizer. In this case the general expression in (2-28) becomes

$$T = \left[X \cos\left(-\boldsymbol{z}_2 + \boldsymbol{a}\right) + Z \sin\left(-\boldsymbol{z}_2 + \boldsymbol{a}\right)\right]^2 + \left[Y \cos\left(\boldsymbol{z}_2 - \boldsymbol{a} - 2\boldsymbol{Y}_D\right)\right]^2 \quad (2\text{-}30)$$

Thus, we plot the measured data and the theoretical calculations with negative and with positive twist angle. As we show in Figure 2.17 for data taken at 633 nm, the theoretical curve with the negative twist is the one that overlaps the measurements.
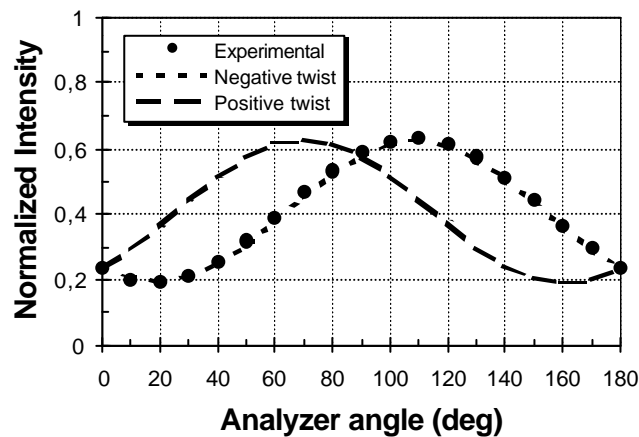

Figure 2.17. Determination of the sign of the twist angle.

For the ambiguity in $\mathbf{Y}_D$ we use the procedure proposed by Davis *et al.* [Dav99b]. We illuminate the LCSLM with linearly polarized light. We address uniform GSL screens to the LCSLM and then we examine the diffraction pattern produced by the pixel structure as a function of the applied voltage. No analyzer is used in the experiment. When the polarized light impinges with the electric field parallel to the director axis in the input face we observe changes in the relative intensities in the diffraction pattern. In Figure 2.18 we can see that for GSL = 200 the diffracted orders pointed by the arrows have an intensity which is clearly different to the intensity for GSL = 250. These differences are even more evident when observed in the laboratory.

In Figure 2.19 we show the images obtained for the diffraction pattern when the light impinges linearly polarized perpendicular to the director axis. They correspond to the same GSLs of Figure 2.18, GSL=200 and GSL=250. We can see that there are no differences in the diffraction pattern at these two GSLs. The same comment can be made for the rest of the GSLs.

Davis *et al.* [Dav99b] proposed a theoretical explanation for this phenomenon. They explain that the changes in the relative intensities for the diffracted spots is caused by an electric field gradient across each pixel. This electric field gradient would cause a gradient in the tilt angle $\mathbf{q}$ for the liquid crystal molecules. While the tilt angle gradient does not affect the ordinary index n_o of refraction, it causes a refractive index gradient for the extraordinary index of refraction n_e across each pixel. As a consequence, there is an optical path gradient across each pixel for incident light polarized along the director. This optical path gradient can be viewed as a blazed grating with a phase profile that acts on the incident light polarized along the director. When we change the voltage applied to the LCSLM, then the electric field gradient is modified. This produces a new phase profile for the blazed grating that generates a different distribution of intensities among the diffracted orders for incident light polarized along the director.
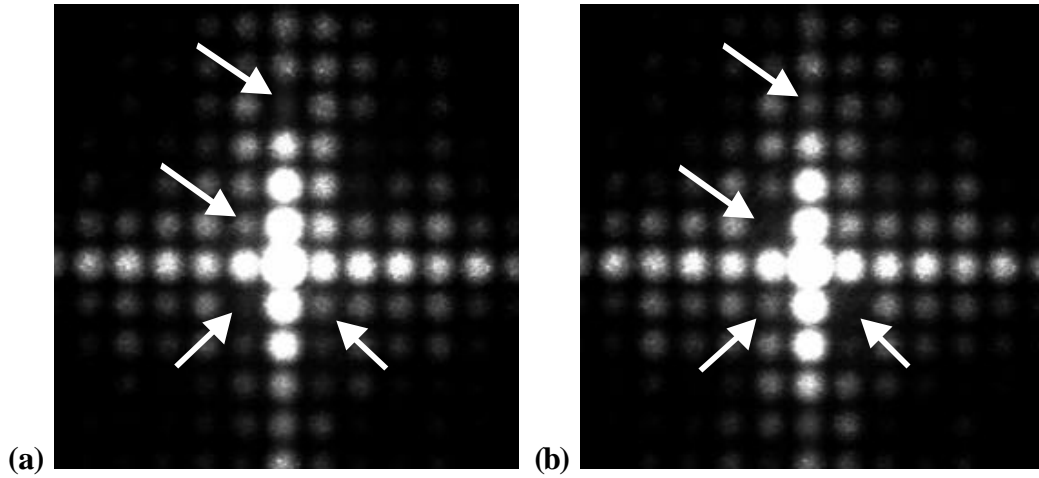
Figure 2.18. Diffraction pattern of the pixelated structure of the LCSLM for incident light linearly polarized parallel to the director axis at the input face. (a) GSL=200, (b) GSL=250.
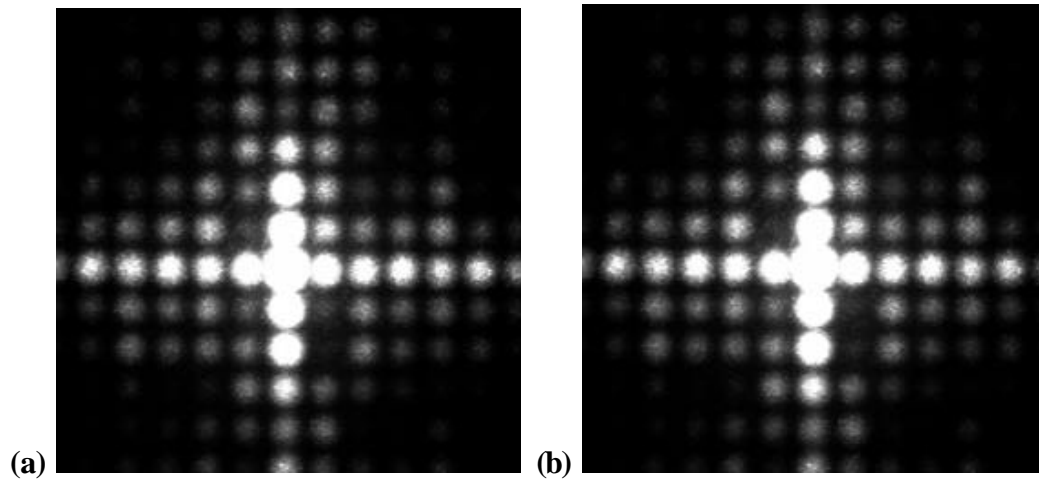
Figure 2.19. Diffraction pattern of the pixelated structure of the LCSLM for incident light linearly polarized perpendicular to the director axis at the input face. (a) GSL=200, (b) GSL=250.

In Table 2.1 we summarise the results that we have obtained for the values of the unknowns according to the different experimental techniques that we have explained along this Section 2.2.2.

α (degrees)	Ψ_D (degrees)	β_{max} (degrees)			
		633 nm	514 nm	488 nm	458 nm
−92	+46	147	193	208	231

Table 2.1. Values of the parameters for the LCSLM used in the experiments.

We have compared the values in Table 2.1 with the values of the parameters obtained with other 9 Sony LCSLMs that we have measured, corresponding to the models LCX012AL and LCX012BL. In particular we have calculated the ratios $b_{max}(\lambda)/b_{max}(633$ nm$)$ at the four wavelengths. In all the LCSLMs the experimental ratios obtained are equal to 1.3, 1.4 and 1.56 respectively for the 514 nm, 488 nm and 458 nm wavelengths compared with the 633 nm wavelength. These values will be used in Section 2.2.4.

Using the ratios $b_{max}(\lambda)/b_{max}(633$ nm$)$ we can obtain interesting information about the optical properties for the LC material used to fill the cell. We know that the expression for the birefringence in the field-off state is given by $b = \pi d \Delta n_{max}/\lambda$ where d is the total thickness of the LC cell and the index difference Δn_{max} depends on the wavelength λ. Then the ratio $b_{max}(\lambda)/b_{max}(633$ nm$)$ can be written as

$$\frac{b_{max}(\lambda)}{b_{max}(633nm)} = \frac{633}{\lambda}\frac{\Delta n_{max}(\lambda)}{\Delta n_{max}(633nm)} \tag{2-31}$$

and we can calculate the normalized dispersion relation $\Delta n_{max}(\lambda)/\Delta n_{max}(633$ nm$)$. This is a specific characteristic of the particular LC material used to fill the cell. The ratios obtained are 1.06, 1.08 and 1.13 respectively for the 514 nm, 488 nm and 458 nm wavelengths compared with the 633 nm wavelength. We observe that the index difference increases as the wavelength decreases.

2.2.3 Intensity and phase measurement set-ups

For the intensity transmission measurement as a function of GSL we use the set-up shown in Figure 2.20 with the LCSLM inserted between the corresponding polarizing devices, in this case two polarizers. This is the same set-up used in the previous Section but now the angles of the polarizers are fixed and it is the addressed GSL that is varied. We use an unexpanded linearly polarized laser beam. The laser beam passes through a wave plate which rotates the incident light and orientates it adequately for the first polarizer P1. We address uniform

GSL images to the LCSLM. A photometer reads the intensity transmitted by the system for the GSL addressed. This data is transferred to a personal computer through an analog/digital converter card. The data is normalized to a maximum value of 1. For normalization purposes we measure at each GSL the intensity transmitted by the system with the analyzer in the orthogonal orientation to the desired one. The addition of the two intensities at each GSL is equal to the total intensity behind the analyzer. This is the normalization value we use for each GSL, thus the normalized value is not affected by the fluctuations in the laser intensity. Note that the photometer takes intensity measurements. If we are interested in the modulus of the amplitude transmission we simply have to calculate the square root of the intensity transmission.
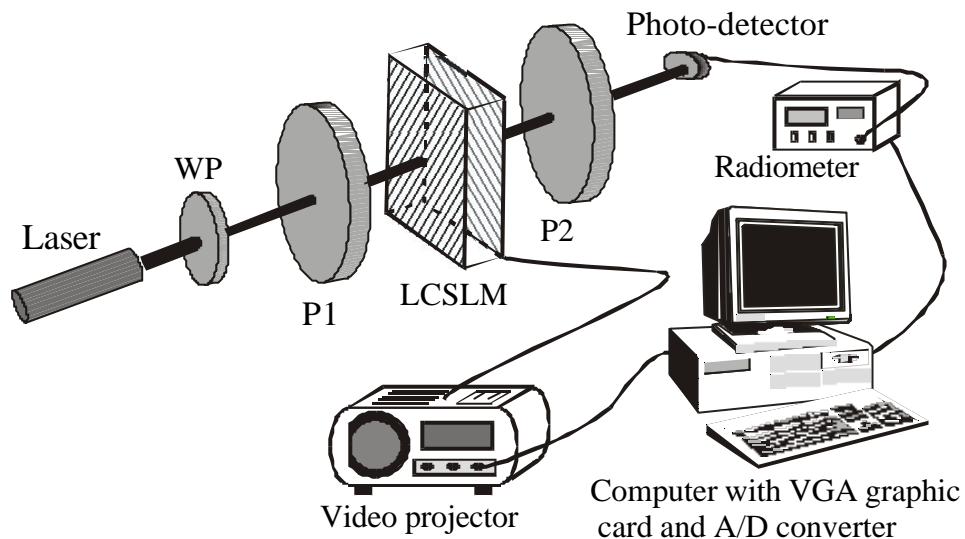
Figure 2.20. Intensity transmission measurement set-up: P1 and P2 are polarizers and WP is a wave plate.

In order to measure the phase modulation as a function of the GSL we use the set-up shown in Figure 2.21. This set-up is analogous with slight variations to set-ups, based on a two-beams interferometer geometry, used by different researchers [Sou94a,Ber95]. The LCSLM is inserted between the polarizing devices, in this case two polarizers, in the desired configuration. An unexpanded laser beam is diffracted by a low frequency (8 lines/mm) phase diffraction grating. The two diffraction maxima corresponding to the first diffraction orders are incident onto the LCSLM. The rest of the diffraction orders are blocked. The lens

L (focal length=20 cm) recombines the two beams after their passage through the LCSLM. The interference fringes produced are magnified with a microscope objective onto the sensor array of a CCD camera, in order to detect 6-8 periods with the camera. The input aperture of the microscope objective serves as a spatial filter that only transmits the zero-order component of the diffraction pattern produced by the pixel structure of the LCSLM.
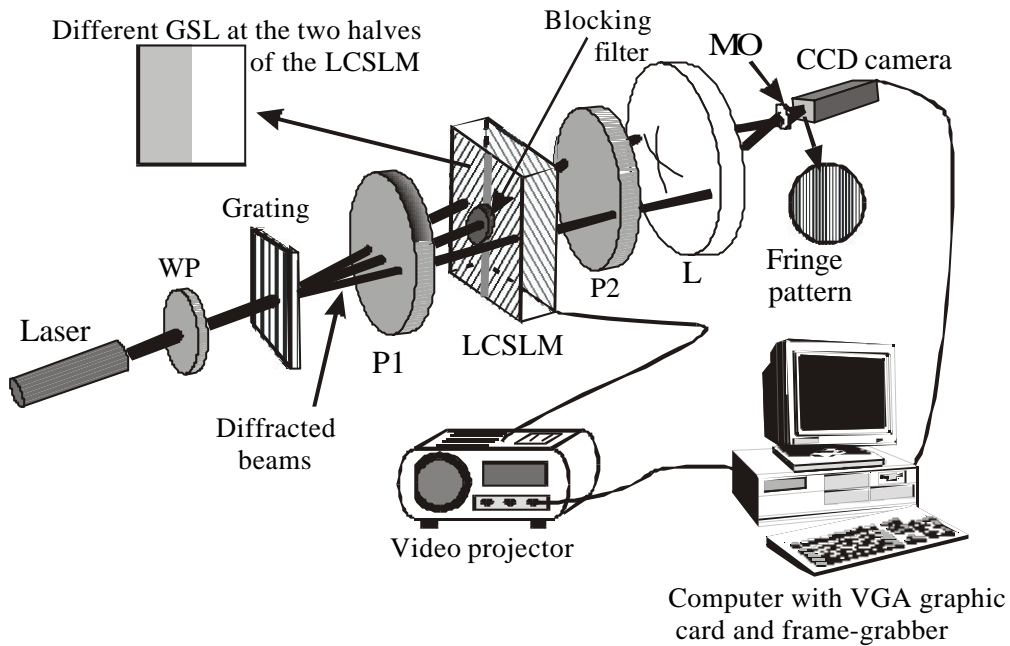
Figure 2.21. Phase modulation measurement set-up: WP is a wave plate, P1 and P2 are polarizers, L is a converging lens, and MO is a microscope objective.

Thus, the pattern produced at the CCD camera is the two-beam interference pattern. The position of this interference fringe pattern on the camera is directly related to the relative phase-shift y between the two beams that form the pattern. It is easily shown that

$$y = 2pD/L \tag{2-32}$$

where D is the interference fringe displacement, and L is the fringe period, both measured in CCD pixels.

The two beams pass through opposite halves of the LCSLM. A different GSL signal is addressed to each half of the LCSLM. Thus, the relative phase-shift y caused by the GSL signals can be obtained by observing the fringe translation.

In order to determine the fringe motion, the image on the CCD camera is captured by a frame-grabber. The software written for this purpose maintains one half of the screen at a constant gray level equal to zero (GSL=0). The GSL at the other half of the screen is changed from GSL = 0 to GSL = 255 in steps of 16 GSL. We acquire an image of the interference fringes at each GSL change as shown in Figure 2.22(a). Each data image is digitally correlated with the first data image acquired, the one that corresponds to the full LCSLM screen at zero GSL. In this way the data is smoothed and at the same time the correlation operation generates a global maximum as we can see in Figure 2.22(b). The displacement in pixels of this correlation peak is equal to the displacement of the fringes D and it is a very precise measurement.
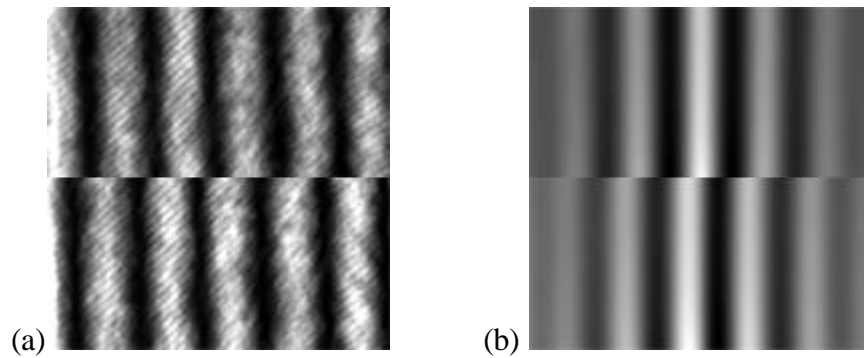
Figure 2.22. Phase measurement experiment in an arbitrary configuration. (a) The upper half shows the fringe pattern captured when the two sides of the screen are at GSL=0. In the lower half we observe the fringe displacement due to the change of GSL in one side of the screen of the LCSLM. (b) The upper half is the autocorrelation calculated using the fringe pattern shown in the upper half of (a). The lower half is the cross-correlation between the two fringe patterns in (a).

2.2.4 Characterization of the voltage dependent edge effect

In [PAPER A] we propose a technique to measure the voltage dependent parameters $b(V)$ and $d(V)$. In this Section we present and analyse this technique with a greater detail.

First of all we study the dependence of both birefringence parameters on the wavelength. They are wavelength dependent parameters, i.e. $b(V, \lambda)$ and $d(V, \lambda)$. In Section 2.2.2 we calculated the values for the ratio $b_{max}(\lambda)/b_{max}(633$

nm) corresponding to the birefringence in the field-off state. Now we will proof that the birefringence ratios keep the same constant value for any applied voltage in the field-on state, i.e.

$$\frac{\boldsymbol{b}_{max}(\boldsymbol{l})}{\boldsymbol{b}_{max}(633nm)} = \frac{\boldsymbol{b}(V,\boldsymbol{l})}{\boldsymbol{b}(V,633nm)} = \frac{\boldsymbol{d}(V,\boldsymbol{l})}{\boldsymbol{d}(V,633nm)} \tag{2-33}$$

or

$$\frac{\boldsymbol{D}n_{max}(\boldsymbol{l})}{\boldsymbol{D}n_{max}(633nm)} = \frac{\boldsymbol{D}n(V,\boldsymbol{l})}{\boldsymbol{D}n(V,633nm)} = \frac{\left\langle \boldsymbol{D}n(V,\boldsymbol{l}) \right\rangle_{d'_1}}{\left\langle \boldsymbol{D}n(V,633nm) \right\rangle_{d'_1}} \tag{2-34}$$

where we have used the more general relation in Eq. (2-13) for $\boldsymbol{d}(V)$. If we are able to proof that Eq. (2-34) is valid, then we simply need to calculate the birefringences $\boldsymbol{b}(V)$ and $\boldsymbol{d}(V)$ for a particular wavelength (e.g. 633 nm). We use the scale factor given by the ratio $\boldsymbol{b}_{max}(\lambda)/\boldsymbol{b}_{max}(633$ nm) to obtain the values at other wavelength.

In order to prove the equality in Eq. (2-34), we remember that a change in the voltage produces a change in the tilt angle $\boldsymbol{q}$. The extraordinary index of refraction $n_e(\boldsymbol{q})$ varies with the tilt angle $\boldsymbol{q}$ according to Eq. (1-3). We consider typical values $n_o=1.5$ and $n_e=1.7$ for the ordinary and extraordinary index of refraction of a nematic liquid crystal at 633 nm. Thus, using the scale factor $\boldsymbol{D}n_{max}(458$ nm)/$\boldsymbol{D}n_{max}(633$ nm)=1.13 calculated in Section 2.2.2, we obtain $n_o=1.5$ and $n_e=1.726$ at 458 nm. Applying these values and using Eq. (1-3) we can simulate the ratio $\boldsymbol{D}n(\boldsymbol{q},458$ nm)/$\boldsymbol{D}n(\boldsymbol{q},633$ nm) as a function of the tilt angle $\boldsymbol{q}$. We have calculated this ratio for the whole domain of the tilt angle $\boldsymbol{q}$ ranging from 0° to 90°. The ratio remains practically constant with values ranging between 1.13 and 1.11. Therefore, we have validated Eq. (2-34) and consequently Eq. (2-33) too. This constancy is an important result that we will apply in the technique to calculate the birefringences $\boldsymbol{b}(V)$ and $\boldsymbol{d}(V)$.

The technique proposed in [PAPER A] is based on the nonlinear curve fitting of intensity transmission measured data. We consider the LCSLM inserted

between two linear polarizers as in Figure 2.3. The intensity transmission of the system is given by Eq. (2-24). We consider three different configurations of the polarizers (and also the associated complementary configurations for normalization purposes). The first configuration corresponds to polarizers with their transmission axes orientated at angles ($\boldsymbol{j}_1 = 0, \boldsymbol{j}_2 = 90$). The complementary configuration, which had been analyzed in Section 2.1.2.2, is ($\boldsymbol{j}_1 = \boldsymbol{j}_2 = 0$). In the second configuration the transmission axes of the polarizers are at angles ($\boldsymbol{j}_1 = 45$, $\boldsymbol{j}_2 = -45$). Its complementary configuration, analyzed in Section 2.1.2.2, is given by the angles ($\boldsymbol{j}_1 = \boldsymbol{j}_2 = 45$). A third configuration ($\boldsymbol{j}_1 = 22.5, \boldsymbol{j}_2 = 112.5$), and its complementary ($\boldsymbol{j}_1 = \boldsymbol{j}_2 = 22.5$) have also been considered. The analytical expressions for the configurations considered in the nonlinear curve fitting are given by

$$T\left(\boldsymbol{j}_1 = 0, \boldsymbol{j}_2 = 90\right) = Z^2 = \frac{\boldsymbol{a}^2}{\boldsymbol{g}^2} sin^2 \boldsymbol{g} \qquad (2\text{-}35a)$$

$$T\left(\boldsymbol{j}_1 = 45, \boldsymbol{j}_2 = -45\right) = 1 - X'^2 = 1 - \left(cos\boldsymbol{g} cos 2\boldsymbol{d} - \frac{\boldsymbol{b}}{\boldsymbol{g}} sin\boldsymbol{g} sin 2\boldsymbol{d} \right)^2 \qquad (2\text{-}35b)$$

$$T\left(\boldsymbol{j}_1 = 22.5, \boldsymbol{j}_2 = 112.5\right) = Z^2 + \frac{Y'^2}{2} =$$
$$= \frac{1}{2}\left\{ \frac{sin^2 \boldsymbol{g}}{\boldsymbol{g}^2}\left(2\boldsymbol{a}^2 + \boldsymbol{b}^2 cos^2 2\boldsymbol{d}\right) + cos^2 \boldsymbol{g} sin^2 2\boldsymbol{d} + \frac{\boldsymbol{b}}{\boldsymbol{g}} sin2\boldsymbol{g} sin4\boldsymbol{d} \right\} \qquad (2\text{-}35c)$$

The first configuration *T(0,90)* is equivalent to the one used by Zhisheng *et al.* [Zhi98] to fit the birefringence of the LCSLM as a function of the applied voltage. They chose this configuration for simplicity in the calculations. They used the Lu and Saleh model, i.e. no edge effect was considered. Nevertheless, this configuration presents an interesting property that we studied in Figure 2.10: the intensity transmission depends on the $\boldsymbol{b}$ birefringence and it does not depend on the $\boldsymbol{d}$ birefringence. Thus, this is a particularly interesting configuration to fit the $\boldsymbol{b}$ birefringence. On the other hand, the second configuration *T(45,-45)* is very

sensitive to the existence of the edge effect as we saw in Figure 2.11. This configuration gives information for calculating the *d* birefringence.

In principle, we can fit the *b* birefringence using Eq. (2-35a) and, then, introduce the relation *b(V)* in expression (2-35b) to calculate the remaining unknown *d(V)*. However, the accuracy of this method decreases as the *b* birefringence increases: for *b* values higher than approximately *150* deg. Eq. (2-35a) is not very sensitive. To assure a greater accuracy in the fitted relations *b(V)* and *d(V)* we have followed a different procedure. We have introduced the third configuration *T(22.5,112.5)* because it presents a higher sensitivity in the region where Eq. (2-35a) is not very sensitive (we will see this point when presenting the experimental results). According to Eq. (2-33), which links the different wavelengths, the addition of more wavelengths does not increase the number of unknowns. Therefore, for maximum accuracy we have made measurements for the three experimental configurations at the same four wavelengths discussed in previous Sections. We use the values of the ratios $b_{max}(\lambda)/b_{max}(633$ nm) to scale the values of *b(V)* and *d(V)* for the different wavelengths. A simultaneous nonlinear curve fitting of the 12 experimental curves has been carried out. We look for the set of values of *b(V)* and *d(V)* that minimizes the square of the difference between the experimental data and the calculated data obtained with Eq. (2-35a), (2-35b) and (2-35c).

For the intensity measurements we have used the set-up shown in Figure 2.20. All the experiments were conducted with the brightness and contrast controls of the video projector at 50 and 100 respectively. We have measured the intensity at intervals of 10 gray levels. In Figure 2.23 we show the experimental data (symbols) obtained with the three configurations and for the four wavelengths. In the same figures we show the corresponding curves obtained in the fitting procedure (continuous line). The horizontal axis shows the GSL that is sent to the LCSLM. For the last data point we switch off the video projector (LCSLM in the field-off state).

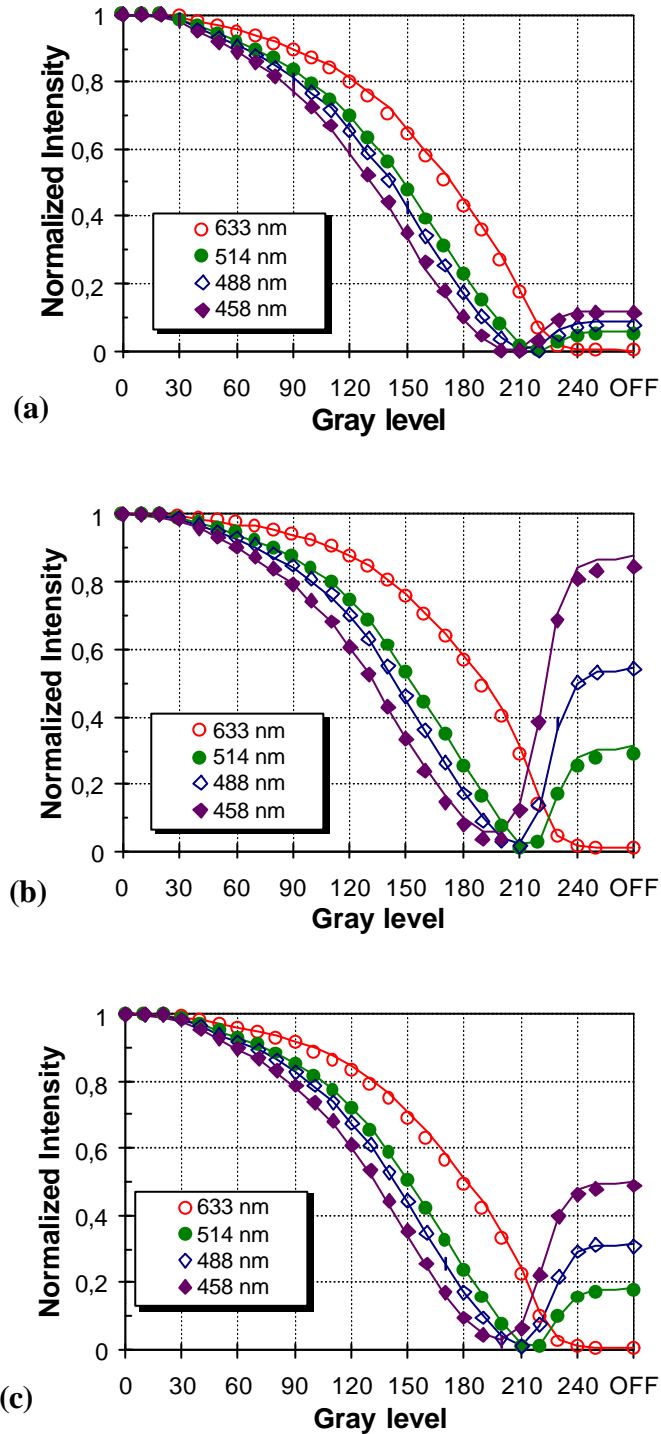**Figure 2.23.** Normalized intensity measurements (symbols) and fitting curves (continuous line) for the three configurations of the polarizers chosen for the fitting procedure. (a) ($j_1=0, j_2=90$), (b) ($j_1=45, j_2=-45$), (c) ($j_1=22.5, j_2=112.5$).

In Figure 2.23(a) the experimental data are shown for the first configuration ($j_1=0, j_2=90$). This data is insensitive to the existence of the edge

layers and shows the characteristic attenuated oscillatory behaviour already commented in Section 2.1.2.2. In Figure 2.23(b) and Figure 2.23(c), we show the measurements for the $(\pmb{j}_1=45, \pmb{j}_2=-45)$ and the $(\pmb{j}_1=22.5, \pmb{j}_2=112.5)$ configurations respectively. The effects of the edge layers are evident in Figure 2.23(b), especially for the 458 nm wavelength. The edge effect causes that the minimum near the GSL 200 is not a zero. In Figure 2.23(c) we can see that at high GSLs this curve presents a larger variation than the first configuration, thus, it can be an appropriate configuration to provide more sensitivity to determine $\pmb{b}(V)$.

We observe in Figure 2.23 that for high GSLs (low values of the voltage) all the curves attain a saturation behavior and they reach an intensity transmission value equal to the intensity measured in the field-off state. The reason is that for these gray levels the voltage is lower than the Freedericksz voltage, at which the LC molecules are perpendicular to the twist axis. On the other side of the horizontal axis in Figure 2.23(a), at GSL=0 the intensity value is equal to one. This corresponds to an applied voltage equal or higher than the saturation voltage, at which all the molecules but the ones in the edge layers are totally tilted. Thus, at brightness=50 and contrast=100 we are covering all the modulation range available with the LCSLM.

The Solver routine in Microsoft Excel has been used for the nonlinear curve fitting. In Figure 2.23 we can see that the fitting curves obtained are in a very good agreement with the experimental data points. In Figure 2.24(a) and Figure 2.24(b) respectively we show the set of values obtained for the birefringences $\pmb{b}(V)$ and $\pmb{d}(V)$ at the four wavelengths. We remember that there is a scale factor that links the corresponding values at the different wavelengths.

In Figure 2.24(a), the $\pmb{b}$ values increase monotonously with GSL. At GSL=0, $\pmb{b}$ is approximately zero. Thus, the LC molecules in the central region of the LCSLM are totally tilted, and the applied voltage exceeds the saturation voltage as we had supposed. Above GSL=230, $\pmb{b}$ reaches the field-off state value

as expected. This confirms that the applied voltage is lower than the Freedericksz threshold. At 458 nm, the birefringence **b** ranges from 0 to 231 degrees.
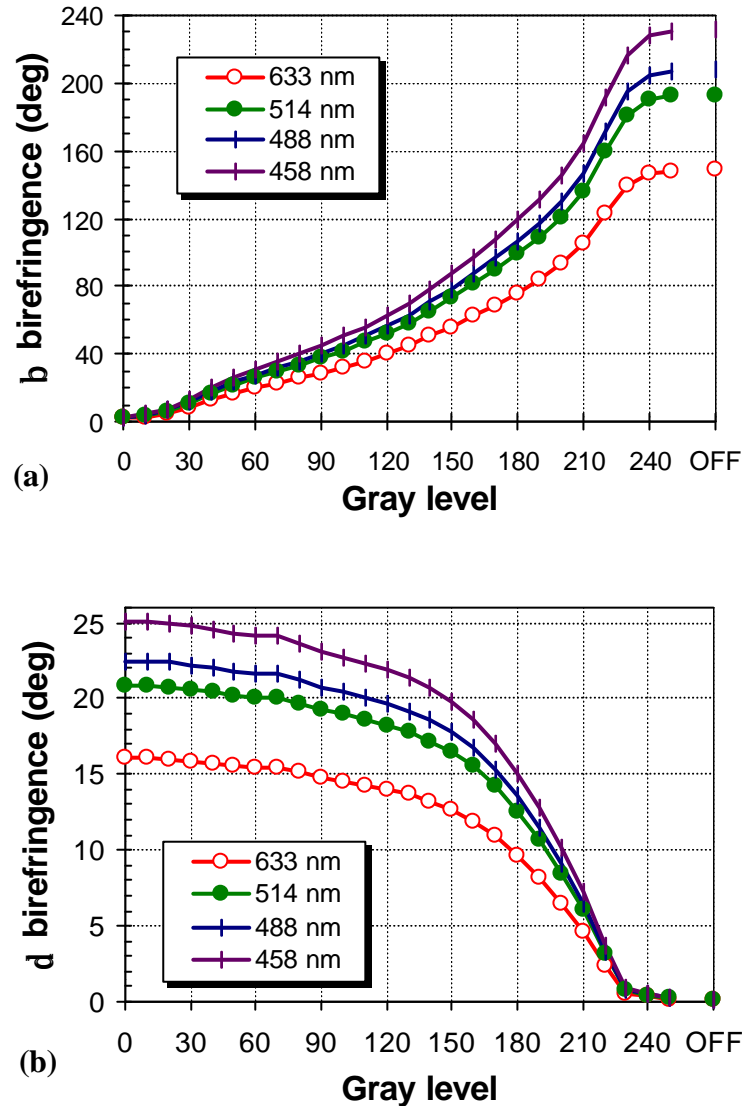
Figure 2.24. Values obtained for the voltage dependent parameters at the four wavelengths. (a) *b(V)*, (b) *d(V)*.

In Figure 2.24(b), at the field-off state point **d** is nearly zero. This confirms that in the field-off-state no edge effect exists and the assumptions made by Yariv and Yeh to obtain Eq. (2-5) are correct. The **d** birefringence increases with the increase in the applied voltages (decrease in the GSLs), achieving a maximum value **d**$_{max}$ of approximately 25 degrees (458 nm). If we calculate the ratio 2**d**$_{max}$/**b**$_{max}$ we obtain that the maximum thickness of the two edge layers represent

a 22% of the total thickness of the LCSLM. We have found values around a 20% with other Sony LCSLMs. These percentages are significant enough for the edge effect to be considered in the proposed model.

2.2.5 Accuracy of the proposed model

The complete knowledge of $\boldsymbol{b}(V)$ and $\boldsymbol{d}(V)$ allows the calculation of the intensity transmission curves for any other configuration. To show this point let us consider an arbitrary configuration $(\boldsymbol{j}_1=0, \boldsymbol{j}_2=45)$. The intensity transmission expression for this particular configuration is given by

$$T(\boldsymbol{j}_1=0,\boldsymbol{j}_2=45)=0.5-X'Z=0.5-\frac{\boldsymbol{a}}{\boldsymbol{g}}sin\boldsymbol{g}\left(cos\,\boldsymbol{g}cos\,2\boldsymbol{d}-\frac{\boldsymbol{b}}{\boldsymbol{g}}sin\boldsymbol{g}sin2\boldsymbol{d}\right)(2\text{-}36)$$
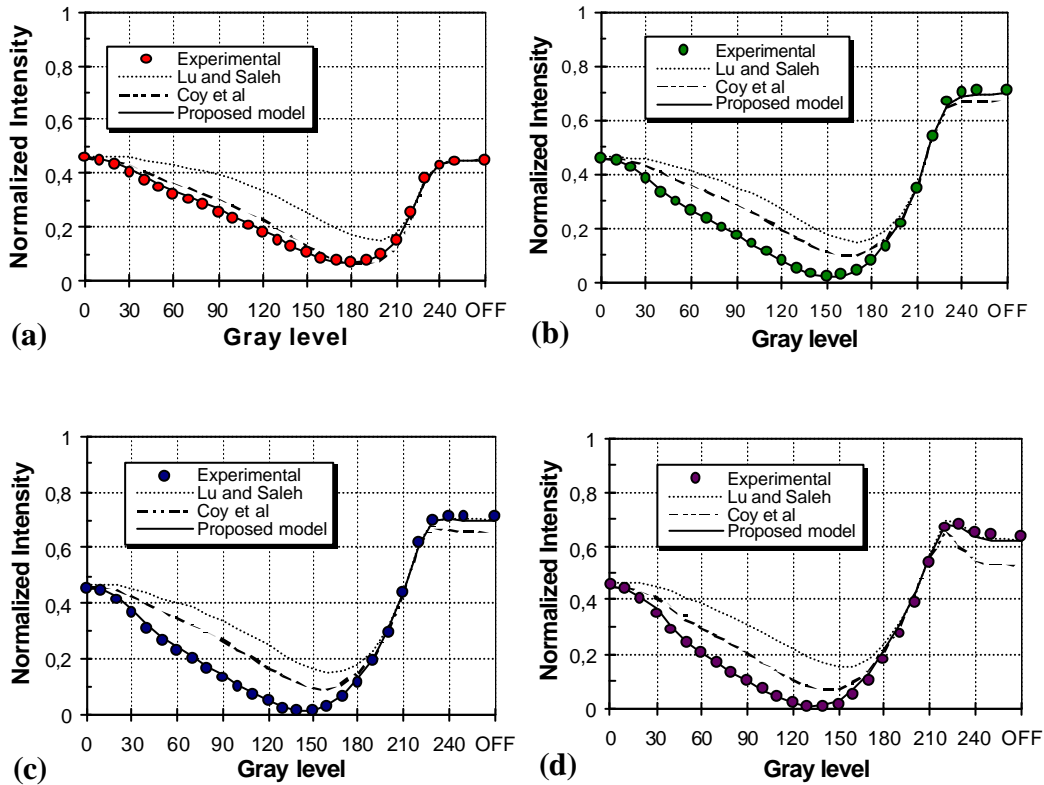

Figure 2.25. Experimental measurements and theoretical intensity transmission curves calculated with the three inverse models: Lu and Saleh, Coy *et al.*, and the model proposed in this thesis. (a) 633 nm, (b) 514 nm, (c) 488 nm, (d) 458 nm.

In Figure 2.25 we show the experimental measurements (symbols) and the theoretical curves (lines) for the four wavelengths (633, 514, 488 and 458 nm, in Figure 2.25(a), (b), (c), and (d) respectively). The three different lines show the theoretical curves calculated using the different models.

The Lu and Saleh model shows the least agreement with the experimental data. In the case of the Coy *et al.* model, the best fit to the experimental is obtained using the constant values $\boldsymbol{d}$ = 9.5º, 5.3º, 5.8º, 8.9º for wavelengths 633, 514, 488, 458 nm respectively. The agreement is improved, but it is not good enough to provide accurate optical transmission calculations. Clearly the calculations made with the model we have proposed in this thesis coincide perfectly with the experimental data. The excellent agreement validates the model and the characterization technique proposed to obtain the relations $\boldsymbol{b}(V)$ and $\boldsymbol{d}(V)$. The voltage dependent edge layers reproduce the effect of the nonlinearities existing in the twist and tilt distributions in the LCSLM.

2.3 Complex transmittance prediction

We have demonstrated that we can measure the parameters $\boldsymbol{b}(V)$ and $\boldsymbol{d}(V)$ which, according to the model we propose, characterize totally the LCSLM operation in the field-on state. We have also demonstrated that using the values for these parameters we are able to simulate the intensity modulation of the LCSLM with a high degree of accuracy. As we said in Section 1.2.3, a certain application requires a specific complex transmittance modulation. Along this Section we demonstrate that we can design optimization procedures which, taking advantage of the accuracy of the model, predict the configurations of the polarizing devices that produce the required modulation.

We know that the LCSLMs produce a coupled amplitude and phase modulation. This coupling is unimportant in display applications because the modulated magnitude is the intensity: the phase modulation curve as a function of the applied voltage can have arbitrary values. Nevertheless, in other applications

the conditions are much more restrictive because the magnitude that we modulate is the complex amplitude transmittance itself, i.e. neither the amplitude nor the phase modulation curves can have arbitrary profiles. Two typical modulation regimes are normally required, phase-only modulation, or amplitude-only modulation. In the comments made for Figure 2.9 and for Figure 2.10 in Section 2.1.2.2 we said that, in the case of a thick LCSLM, these regimes are possible by inserting the LCSLM between polarizers. However, the use of the newer thin LCSLMs, especially in experiments where phase-only modulation is required, impose new difficulties. Here, the typical configuration with the two polarizers does not provide the required performance.

The predictive capability of the model is demonstrated in this Section. We predict phase-only configurations and amplitude-only configurations. We use two new approaches, one of them has been recently proposed by us in [PAPER B]. In Section 2.3.1 we develop the theory for the two approaches, and in Section 2.3.2 and 2.3.3 we present the results.

2.3.1 Generation and detection of polarized light

The amplitude and phase modulation provided by a LCSLM depend on the applied voltage and on the polarization state of the light incident on the LCSLM. In general, the polarization states of light are elliptical [Hua93]. In Figure 2.26 we represent an elliptical polarization state. A polarization state is fully determined through two parameters: the ellipticity e and the azimuth angle W. The ellipticity of the ellipse is defined as the ratio $\pm b/a$ between the lengths of the two axes, where the sign $\pm$ depends on the helicity of the ellipse. The ellipticity is taken as positive when the rotation of the electric field vector is right-handed (clockwise) and we look in the direction of the light going from the laser to the detector. In Figure 2.26 we have expressed left-handed (counter-clockwise light). The azimuth angle W represents the orientation of the principal axes of the ellipse with respect to the laboratory coordinates. Linearly and circularly polarized light are particular

cases of the ellipse with ellipticities **e** = *0* (linearly polarized light) and **e** = *1* (circularly polarized light).
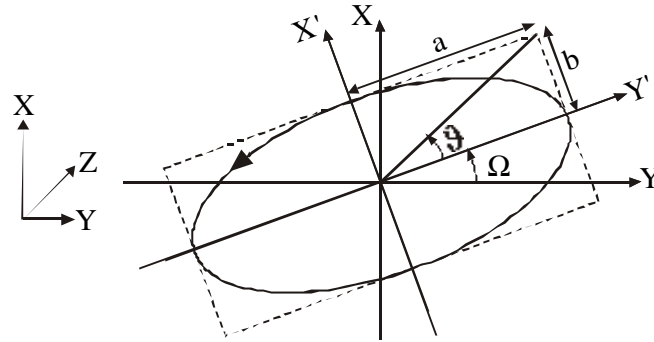

Figure 2.26. Polarization ellipse and its characteristic parameters. The angles **J** and **W** indicated in the figure have a negative value according to the sign convention that we follow in this thesis. The ellipse has a left-handed helicity.

The polarization state in Figure 2.26 with an ellipticiy **e** can be generated using a polarizer followed by a quarter-wave plate (QWP). We orientate the quarter-wave plate (QWP) with its slow axis parallel to the *X'* principal axis of the ellipse that we want to generate. The polarizer has its transmission axis at an angle **J** with respect to the *Y'* principal axis of the ellipse (see Figure 2.26). The angle **J** is related with the ellipticity of the ellipse,

$$\mathbf{J} = atan\,\mathbf{e} \tag{2-37}$$

Until now we have seen the LCSLM inserted between two polarizers. In this situation the LCSLM is working with linearly polarized light. In Section 2.3.1.1 we show the possibility of using the polarization eigenstates of the LCSLM. In Section 2.3.1.2 we develop a general theory, that includes the eigenstates as a particular case, to use arbitrary elliptically polarized states of light.

2.3.1.1 Eigenvectors and eigenvalues of the LCSLM

As said in Section 1.2.3, the eigenvectors of the LCSLM have been investigated to provide phase-only modulation. Two different kinds of eigenvectors are defined by Davis *et al.* [Dav98]: the classic eigenvectors and the

rotated eigenvectors. We rewrite the expression for the Jones matrix $M'_{LCSLM}($**a,b,d**$)$ of the LCSLM (Eq. (2-16)) as follows

$$M'_{LCSLM}\left(\boldsymbol{a},\boldsymbol{b},\boldsymbol{d}\right)=exp\left(-i\left(\boldsymbol{b}+2\boldsymbol{d}\right)\right)R\left(-\boldsymbol{a}\right)M\left(\boldsymbol{a},\boldsymbol{b},\boldsymbol{d}\right) \tag{2-38}$$

where $M($**a,b,d**$)$ is given by

$$M\left(\boldsymbol{a},\boldsymbol{b},\boldsymbol{d}\right)=\begin{pmatrix} X'-iY' & Z \\ -Z & X'+iY' \end{pmatrix} \tag{2-39}$$

The classic eigenvectors are obtained with the diagonalization of the Jones matrix of the LCSLM $M'_{LCSLM}($**a,b,d**$)$. The rotated eigenvectors are obtained with the diagonalization of the matrix $M($**a,b,d**$)$. In the following we will focus on the rotated eigenvectors. They are the interesting ones for phase-only modulation.

An input eigenvector $\vec{E}_s$ having an eigenvalue **s** for the matrix $M($**a,b,d**$)$ is defined as

$$M\left(\boldsymbol{a},\boldsymbol{b},\boldsymbol{d}\right)\vec{E}_s =\boldsymbol{s}\vec{E}_s \tag{2-40}$$

Solving Eq. (2-40) we get the two eigenvalues $\boldsymbol{s}_\pm$,

$$\boldsymbol{s}_\pm =\pm\boldsymbol{s} \tag{2-41}$$

where **s** is given by

$$\boldsymbol{s} = atan\left(\frac{\sqrt{1-X'^2}}{X'}\right) \tag{2-42}$$

If we look at Eq. (2-38), as the eigenvectors $\vec{E}_{s\pm}$ propagate through the LCSLM, they are rotated by the rotation matrix $R(-$**a**$)$ and receive phase-shifts $\boldsymbol{y}_\pm$ given by

$$\boldsymbol{y}_\pm = -\left(\boldsymbol{b}+2\boldsymbol{d}\mp\boldsymbol{s}\right) \tag{2-43}$$

In the following we do not take into account the overall sign in Eq. (2-43). We can see that the negative eigenvector $\vec{E}_{s-}$ receives a larger phase-shift $\boldsymbol{y}_-$ of $\left(\boldsymbol{b}+2\boldsymbol{d}+\boldsymbol{s}\right)$ while the positive eigenvector $\vec{E}_{s+}$ receives a much smaller phase-

shift $\mathbf{y}_+$ of $(\mathbf{b} + 2\mathbf{d} - \mathbf{s})$, where $\mathbf{b}$, $\mathbf{d}$, and $\mathbf{s}$ are magnitudes with positive values. The normalized eigenvectors $\vec{E}_{\mathbf{s}-}$, $\vec{E}_{\mathbf{s}+}$ are given by

$$\vec{E}_{\mathbf{s}+} = \frac{1}{N}\begin{pmatrix} Z \\ i\left(Y' + \sqrt{1 - X'^2}\right) \end{pmatrix} \tag{2-44a}$$

$$\vec{E}_{\mathbf{s}-} = \frac{1}{N}\begin{pmatrix} Y' + \sqrt{1 - X'^2} \\ -iZ \end{pmatrix} \tag{2-44b}$$

$$N = \sqrt{2 - 2X'^2 + 2Y'\sqrt{1 - X'^2}} \tag{2-45}$$

where N is the normalization factor. We remember that the eigenvectors are orthogonal to each other. We can see that the components of the eigenvectors are dephased an angle of 90°. These eigenvectors represent elliptically polarized light centered along the director of the LCSLM in the input side. The transmitted eigenvector has exactly the same ellipticity as the incident eigenvector. However the major and the minor axes are rotated by the twist angle $\mathbf{a}$ of the LCSLM.

In the case with no edge effect the expressions for the eigenvalues and eigenvectors are greatly simplified:

$$\mathbf{s}_{\pm} = \pm\mathbf{g} \tag{2-46a}$$

$$\vec{E}_{\mathbf{s}+} = \frac{1}{\sqrt{2\mathbf{g}(\mathbf{b}+\mathbf{g})}}\begin{pmatrix} \mathbf{a} \\ i(\mathbf{b}+\mathbf{g}) \end{pmatrix} \tag{2-46b}$$

$$\vec{E}_{\mathbf{s}-} = \frac{1}{\sqrt{2\mathbf{g}(\mathbf{b}+\mathbf{g})}}\begin{pmatrix} (\mathbf{b}+\mathbf{g}) \\ -i\mathbf{a} \end{pmatrix} \tag{2-46c}$$

The helicity of these eigenvectors depend on the sense of the twist angle $\mathbf{a}$ for the LCSLM. We remember that the angles are taken to be positive when the sense is clockwise (looking in the direction of the light going from the laser to the detector). We can see that the helicity of the negative eigenvector has the same sense as the twist angle.
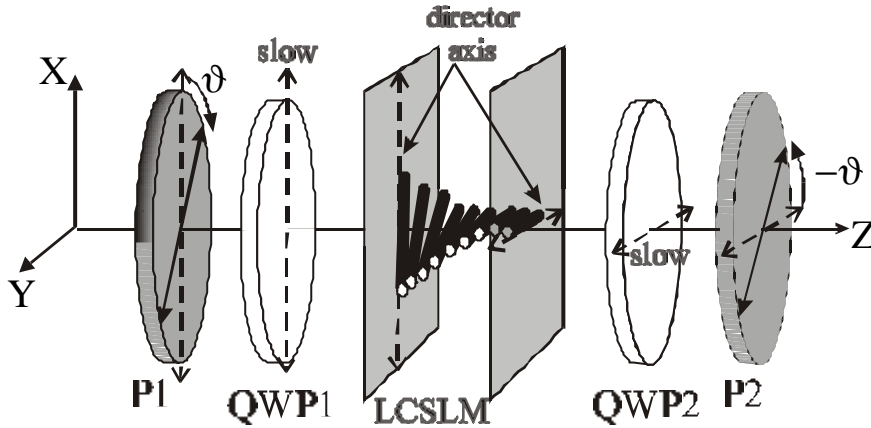
Figure 2.27. Scheme for the set-up to generate and detect the eigenvectors.

In Figure 2.27 we show the set-up to generate and to detect an eigenvector of the LCSLM. Linearly polarized light produced by the polarizer P1 is incident on the quarter-wave plate QWP1. The slow axis of QWP1 is parallel to the director at the input face of the LCSLM. The angle J between the polarization direction of the incident light and the slow axis of QWP1 determines the ellipticity of the elliptically polarized light that is incident upon the input face of the LCSLM, as indicated by Eq. (2-37). At the output of the LCSLM, we need to transform the transmitted eigenvector into linearly polarized light. For this purpose the quarter-wave plate QWP2 has its slow axis parallel to the director axis at the output face of the LCSLM. At the output QWP2 we have linearly polarized light at an angle -J with respect to the slow axis of the QWP2. This is the orientation for the polarizer P2.

By definition the amplitude of the eigenvector does not change when traversing the LCSLM. Thus, in principle we can obtain a perfect phase-only modulation. Nevertheless, the eigenvectors vary with the voltage due to the dependence of the matrix $M(a,b,d)$ on the two voltage dependent parameters $b(V)$ and $d(V)$. Thus, the ellipticity e of the eigenvector and consequently the angle J to generate and detect the eigenvector are not constants over a certain voltage range. In practice, we have to use the concept of the average eigenvector [Dav98]. The average eigenvector is defined as the eigenvector that provides the most uniform transmission over a given voltage range for the LCSLM. From this definition we

can see that, actually, the average eigenvector is not obtained through any averaging calculation. It is simply the best eigenvector according to the criterion of most uniform tranmission along the whole voltage range. The average eigenvector is generated and detected with the set-up shown in Figure 2.27 taking into account that the angles of the input and output polarizers, P1 and P2, are restricted to be symmetrical, $\boldsymbol{J}$ and $-\boldsymbol{J}$ respectively, with respect to the slow axes of the quarter-wave plates QWP1 and QWP2.

In Section 2.3.1.2 we develop a more general approach to manipulate elliptically polarized light with a LCSLM that includes the case of the eigenvectors and the average eigenvector as a particular case.

2.3.1.2 General elliptically polarized states of light

The most general architecture consists in inserting the LCSLM between two sets formed by a linear polarizer and a wave plate. We consider that we can rotate arbitrarily the two wave plates and the two polarizers. We also consider that the wave plates can introduce arbitrary retardance, even though we will see that we are limited by the available wave plates in the laboratory. This architecture provides us with all the possible degrees of freedom in order to look for a desired amplitude or phase modulation. The classical system consisting of two linear polarizers, and the system to generate and detect the polarization eigenstates of the LCSLM are particular cases of this more general architecture.

The scheme for this architecture is presented in Figure 2.28. A wave plate introducing a retardance $2\boldsymbol{f}_1$ is placed between the first polarizer and the LCSLM. A second wave plate introducing a retardance $2\boldsymbol{f}_2$ is placed between the LCSLM and the second polarizer. The angles of the elements in front of the LCSLM are referred to the orientation of the molecular director at the input surface (which we suppose that coincides with the X-coordinate axis). The angle $\boldsymbol{j}_1$ denotes the orientation of the transmission axis of the first polarizer and the angle $\boldsymbol{h}_1$ denotes the orientation of the slow axis of the first wave plate. On the other hand, the angles $\boldsymbol{h}_2$ and $\boldsymbol{j}_2$ correspond to the orientation of the slow axis of the second wave

plate and the transmission axis of the second polarizer. For these two last elements the angles are measured with respect to the orientation of the molecular director at the output surface (i.e. rotated an angle a with respect to the X-coordinate axis).
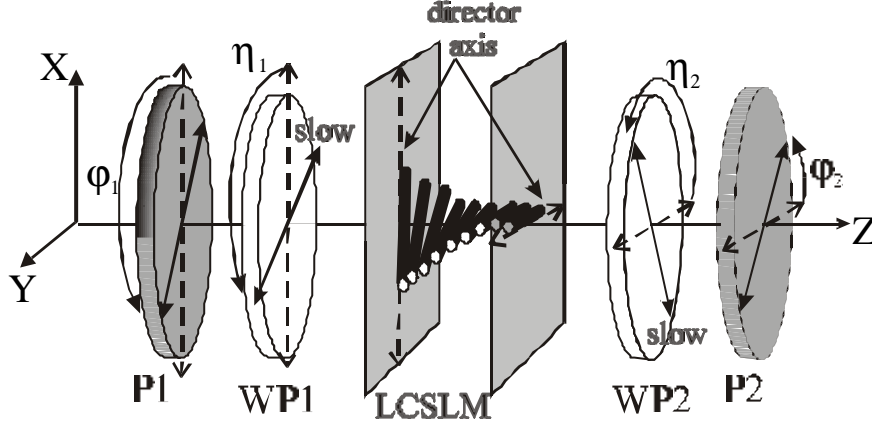

Figure 2.28. Scheme for the generalized elliptical light set-up.

The classical system consisting of two linear polarizers, Figure 2.3, corresponds to the case $2f_1=2f_2=0$. The system to generate and detect the polarization eigenstates of the LCSLM, Figure 2.27, corresponds to the case $2f_1=2f_2=90$ with the restrictions $2h_1=2h_2=0$ and $j_2=-j_1$.

Once again we use the Jones matrix formalism in order to calculate the complex amplitude vector $\vec{E}_{OUT}$ at the end of the optical system,

$$\vec{E}_{OUT} = P_X \cdot R(a+j_2) \cdot R(-a-h_2) \cdot W_0(2f_2) \cdot R(a+h_2)$$
$$\cdot M'_{LCSLM}(a,b,d) \cdot R(-h_1) \cdot W_0(2f_1) \cdot R(h_1) \cdot \begin{pmatrix} cos\,j_1 \\ sin\,j_1 \end{pmatrix} \quad (2\text{-}47)$$

where $R(v)$ and P_X have been already introduced in Eq. (2-6) and (2-19), and $W(2f)$ is the matrix of a wave plate expressed in its proper axes,

$$W(2f) = \begin{pmatrix} exp(-if) & 0 \\ 0 & exp(+if) \end{pmatrix} \quad (2\text{-}48)$$

The resultant complex amplitude of the component E_t transmitted by this system is given by

$$E_t = exp\big(- i(\,\boldsymbol{b} + 2\boldsymbol{d}\,)\big)\big(A_{RE} + iA_{IM}\,\big) \tag{2-49}$$

where A_{RE} and A_{IM} are real magnitudes whose expressions are

$$
\begin{aligned}
A_{RE} = &\ X'\big[cos\boldsymbol{f}_1\,cos\boldsymbol{f}_2\,cos(\boldsymbol{j}_1 - \boldsymbol{j}_2\,) - sin\boldsymbol{f}_1 sin\boldsymbol{f}_2\,cos(2(\boldsymbol{h}_1 - \boldsymbol{h}_2\,) - \boldsymbol{j}_1 + \boldsymbol{j}_2\,)\big]\\
&+ Y'\big[- cos\boldsymbol{f}_1 sin\boldsymbol{f}_2\,cos(2\boldsymbol{h}_2 + \boldsymbol{j}_1 - \boldsymbol{j}_2\,) - sin\boldsymbol{f}_1\,cos\boldsymbol{f}_2\,cos(2\boldsymbol{h}_1 - \boldsymbol{j}_1 + \boldsymbol{j}_2\,)\big]\\
&+ Z\big[cos\boldsymbol{f}_1\,cos\boldsymbol{f}_2 sin(\boldsymbol{j}_1 - \boldsymbol{j}_2\,) - sin\boldsymbol{f}_1 sin\boldsymbol{f}_2 sin(2(\boldsymbol{h}_1 - \boldsymbol{h}_2\,) - \boldsymbol{j}_1 + \boldsymbol{j}_2\,)\big]
\end{aligned}
\tag{2-50a}
$$

$$
\begin{aligned}
A_{IM} = &\ X'\big[- cos\boldsymbol{f}_1 sin\boldsymbol{f}_2\,cos(2\boldsymbol{h}_2 - \boldsymbol{j}_1 - \boldsymbol{j}_2\,) - sin\boldsymbol{f}_1\,cos\boldsymbol{f}_2\,cos(2\boldsymbol{h}_1 - \boldsymbol{j}_1 - \boldsymbol{j}_2\,)\big]\\
&+ Y'\big[- cos\boldsymbol{f}_1\,cos\boldsymbol{f}_2\,cos(\boldsymbol{j}_1 + \boldsymbol{j}_2\,) + sin\boldsymbol{f}_1 sin\boldsymbol{f}_2\,cos(2(\boldsymbol{h}_1 + \boldsymbol{h}_2\,) - \boldsymbol{j}_1 - \boldsymbol{j}_2\,)\big]\\
&+ Z\big[cos\boldsymbol{f}_1 sin\boldsymbol{f}_2 sin(2\boldsymbol{h}_2 - \boldsymbol{j}_1 - \boldsymbol{j}_2\,) - sin\boldsymbol{f}_1\,cos\boldsymbol{f}_2 sin(2\boldsymbol{h}_1 - \boldsymbol{j}_1 - \boldsymbol{j}_2\,)\big]
\end{aligned}
\tag{2-50b}
$$

The intensity transmittance T for this system is obtained as

$$T = A_{RE}^2 + A_{IM}^2 \tag{2-51}$$

and the phase-shift $\boldsymbol{y}$ is given by

$$\boldsymbol{y} = -\boldsymbol{b} - 2\boldsymbol{d} + atan\left(\frac{A_{IM}}{A_{RE}}\right) \tag{2-52}$$

As $\boldsymbol{b}(V)$ and $\boldsymbol{d}(V)$ have already been measured, it is possible to perform a computer search for a desired modulation. In the optimization process we assign initial arbitrary values to the angles $\boldsymbol{h}_1$, $\boldsymbol{h}_2$, $\boldsymbol{j}_1$ and $\boldsymbol{j}_2$, then, the transmittance T and the phase-shift $\boldsymbol{y}$ can be calculated using Eq. (2-51) and (2-52). The optimization criterion to be applied depends on the complex transmittance modulation we are interested on. In case two variable wave plates are available (for instance using Soleil-Babinet compensators), the computation of the search for a desired modulation may also include $\boldsymbol{f}_1$ and $\boldsymbol{f}_2$ as free parameters. In any other case the values of $\boldsymbol{f}_1$ and $\boldsymbol{f}_2$ are fixed by the available wave plates.

For the computer search, arbitrarily we have chosen two available wave plates with a retardance of $2\boldsymbol{f}_1 = 125$ degrees and $2\boldsymbol{f}_2 = 94.5$ degrees respectively for the wavelength 458 nm. The rest of the magnitudes, $\boldsymbol{h}_1$, $\boldsymbol{h}_2$, $\boldsymbol{j}_1$ and $\boldsymbol{j}_2$, are left as free parameters in the optimization process. The case $2\boldsymbol{f}_1 = 2\boldsymbol{f}_2 = 0$ (only polarizers) has also been considered in a new computer search, corresponding to the situation when no wave plates are present.

In another computer search we have considered the case of the average eigenvector, given in Section 2.3.1.1. This case corresponds to the values $2f_1=2f_2=90$ with the restrictions $2h_1=2h_2=0$ and $j_2=-j_1$. Actually, to generate and to detect the average eigenvectors we have used the two available wave plates with closest retardance to a quarter-wave plate for the 458 nm. These two wave plates have a retardance $2f_1 = 88$ degrees and $2f_2 = 94.5$ degrees. We have considered these values in the computer search for the average eigenvector. We remember that the average eigenvector is the eigenvector which provides the most uniform transmission along the whole voltage range.

In the next two Sections 2.3.2 and 2.3.3 we present the experimental measurements obtained for the unexpanded beam of an Ar^+ laser at 458 nm at the predicted configurations. The experimental measurements are compared with the predicted ones.

2.3.2 Accurate prediction of phase-only modulation

An optimum phase-only configuration produces a flat amplitude modulation and a phase modulation with a phase depth of 2π radians. The criterion we follow is to minimize the difference between the maximum and the minimum transmitted intensity $T_{max} - T_{min}$ over the entire voltage range. The intensity transmission may not be maximum, but we are interested in a configuration where it remains constant.

First, we consider the case of the average eigenvectors. As we said in Section 2.3.1.2, this case is given by the restrictions $2h_1=2h_2=0$ and $j_2=-j_1$ in the computer search. We consider the retardances $2f_1 = 88$ degrees and $2f_2 = 94.5$ degrees of the two available wave plates with a closest behavior to quarter wave plates for 458 nm. The two wave plates have their slow axis parallel to the director axis at input and at the output faces of the LCSLM respectively. The result of the optimization search leads to two configurations of the polarizers with the following angles $j_1=-j_2=+29$ degrees and $j_1=-j_2=-61$ degrees respectively.

An interesting result is that the two configurations are orthogonal to each other, thus the two average eigenvectors are orthogonal to each other.

In Table 2.2 we summarise the predicted and the experimental values for the range of variation of the intensity $T_{max} - T_{min}$ and the range of variation of the phase-shift $\boldsymbol{D\psi}$. The value for $T_{max} - T_{min}$ is 25%, that is a good value for a thin LCSLM. We can see that the configuration $\boldsymbol{j}_1 = -\boldsymbol{j}_2 = +29$ presents a large variation of the phase-shift $\boldsymbol{D\psi}$. This is the negative eigenvector and the configuration $\boldsymbol{j}_1 = -\boldsymbol{j}_2 = -61$ corresponds to the positive eigenvector with a very small phase modulation range. Thus, the negative eigenvector can be used to obtain phase-only modulation. The agreement between the predicted and the experimental values for $T_{max} - T_{min}$ and for $\boldsymbol{D\psi}$ is excellent. The only differences, even though not very significant, appear in the magnitude $\boldsymbol{D\psi}$ for the negative eigenvector.

Configuration		$T_{max} - T_{min}$ (%)		$\boldsymbol{D\psi}$ (degrees)	
		Predicted	Experim.	Predicted	Experim.
Negative eigen.	$\boldsymbol{j}_1 = -\boldsymbol{j}_2 = +29$	25	25	331	313
Positive eigen.	$\boldsymbol{j}_1 = -\boldsymbol{j}_2 = -61$	25	25	26	28
Non-symmetric	$\boldsymbol{j}_1 = +11, \boldsymbol{j}_2 = -44$	15	11	337	332

Table 2.2. Predicted and experimental ranges of variation of the intensity and of the phase-shift over the whole voltage range.

We continue with the two wave plates $2\boldsymbol{f}_1 = 88$ degrees and $2\boldsymbol{f}_2 = 94.5$ with their slow axis parallel to the director axis at both faces of the LCSLM respectively. We have performed a new computer search where we do not impose $\boldsymbol{j}_1 = -\boldsymbol{j}_2$: now the angles $\boldsymbol{j}_1$ and $\boldsymbol{j}_2$ of both polarizers are left as free parameters, i.e. this is not an average eigenvector. The predicted configuration has the following angles $\boldsymbol{j}_1 = +11$ and $\boldsymbol{j}_2 = -44$. We see that the computer search does not lead to the average eigenvector geometry $\boldsymbol{j}_1 = -\boldsymbol{j}_2$. We call this new configuration non-symmetric. We can see in Table 2.2 that it provides a lower $T_{max} - T_{min}$ and a larger $\boldsymbol{D\psi}$ than the negative eigenvector. The agreement between the predicted and the experimental values is excellent.

In Figure 2.29 we show the intensity and the phase-shift values over the gray levels applied for the three configurations listed in Table 2.2. We show the experimental values (symbols) and the predicted curves (lines). In Figure 2.29(a) we see the good agreement between predicted and experimental intensities. In the case of the non-symmetric configuration the predicted curve (dashed line) follows the same shape as the experimental data points but slightly shifted. An interesting result is that the predicted intensity for the two eigenvectors (continuous line) is exactly identical. Experimentally measured data points confirm this result. In Figure 2.29(b) the agreement between predicted and experimental phase-shifts is excellent. Furthermore, the phase-shifts for the negative eigenvector and for the non-symmetric configuration increase monotonously and they stay close to 2π radians.
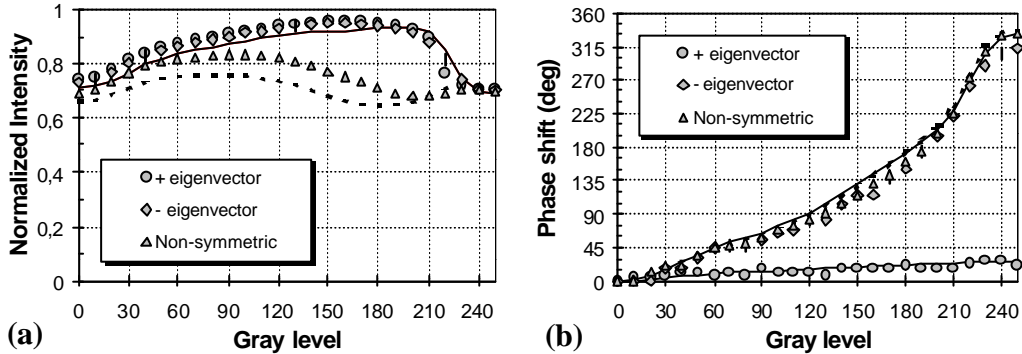

(a)   **(b)**

Figure 2.29. Phase-only modulation. Eigenvectors and non-symmetric configurations. (a) Normalized intensity. (b) Phase-shift. The symbols correspond to experimental measurements. The lines correspond to predicted values: continuous line for the eigenvectors and dashed line for the non-symmetric configuration.

Further analysis has been done to study other possible phase-only configurations. In principle we are interested in taking advantage of the maximum number of degrees of freedom provided by the general set-up in Figure 2.28. We have employed two available wave plates with a retardance of $2f_1 = 125$ degrees and $2f_2 = 94.5$ degrees respectively for the wavelength 458 nm. The rest of the magnitudes, h_1, h_2, j_1 and j_2, are left as free parameters in the optimization process. We also want to perform a comparison with the results that we would expect if no wave plates are present. This means that we have to consider $2f_1 =$

$2f_2 = 0$ in a new computer search. In Table 2.3 we summarise the results obtained when we consider the classical system, with only polarizers, and the general system, with wave plates.

Configuration		$T_{max} - T_{min}$ (%)		$D\psi$ (degrees)	
		Predicted	Experim.	Predicted	Experim.
Only polarizers	$j_1=+22, j_2=-21$	49	50	266	260
General	$j_1=+26, j_2=-16$ $h_1=0, h_2=+11$	4	9	360	348

Table 2.3. Predicted and experimental ranges of variation of the intensity and of the phase-shift over the whole voltage range.

First of all, we remark the high degree of agreement between predicted and experimental results in Table 2.3. As expected for a thin LCSLM, only polarizers provide a very bad performance (50% of intensity variation) for phase-only modulation. For the general configuration with the wave plates the optimum configuration provides an almost ideal phase-only modulation with a uniform intensity transmission and a variation of the phase-shift $D\psi$ of nearly 360 degrees. The intensity variation range is even lower than for the non-symmetric configuration shown in Table 2.2. This is an important result, as it suggests that in general we are not limited to use quarter-wave plates to obtain satisfactory phase-only modulation. Another important result when adding wave plates in comparison with only polarizers, is that we get not only a very uniform transmission but also a large increase, about 90 degrees, in the variation of the phase-shift $D\psi$. Thus, we have demonstrated that we can obtain phase-only modulation with thin LCSLMs by using wave plates and by using short wavelengths.

In Figure 2.30 we show the intensity and the phase-shift values over the gray levels applied for the only polarizers configuration and for the general configuration with wave plates. We show the experimental values (symbols) and the predicted curves (lines).

In both Figure 2.30(a) and Figure 2.30(b) we see the excellent agreement between predicted and experimental values. In Figure 2.30(b) we observe that the evolution of the phase-shift with the GSL is monotonous for both configurations. The linearity is better in the case of the curve for the general configuration.
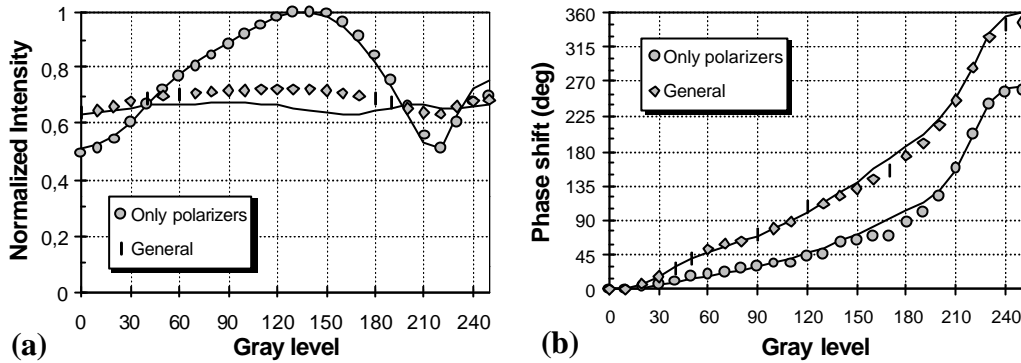

Figure 2.30. Phase-only modulation. Only polarizers and general configurations. (a) Normalized intensity. (b) Phase-shift. The symbols correspond to experimental measurements and the lines correspond to predicted values.
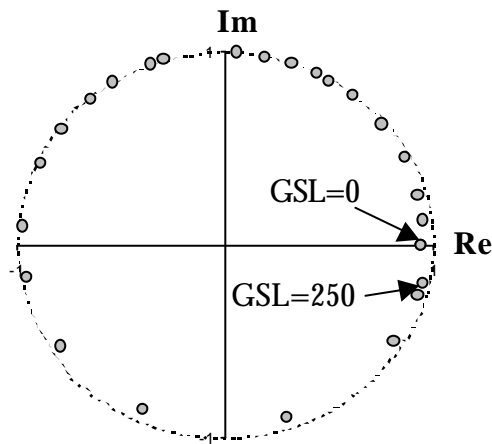

Figure 2.31. Complex plane representation of the phase-only modulation. The symbols correspond to the experimental measurements for the phase-only configuration in the general case with wave plates. The amplitude is normalized to a maximum value of one. The dashed line corresponds to a circle with unit radius.

In the general case with wave plates, we represent in Figure 2.31 the results for the phase-only configuration in the complex plane. In this representation the distance of the experimental points (symbols) to the origin of the coordinate system corresponds to the amplitude transmittance, i.e. the root

square of the intensity, for the corresponding GSL. The amplitude transmittance has been normalized to a maximum value of one. The angle between the experimental point with respect to the real axis corresponds to the phase-shift $\boldsymbol{D\psi}$ for the corresponding GSL. The dashed line indicates a circle with unit radius, that corresponds to an ideal phase-only modulation. We can perceive that the experimental points practically overlap the unit radius circle.

2.3.3 Accurate prediction of amplitude-only modulation

We remember that in the amplitude-only modulation we seek for a configuration that combines the next three features:

➢ flat phase response,

➢ high intensity contrast, and

➢ monotonous and linear intensity transmission response with the GSL.

The intensity contrast is defined as the ratio T_{max}/T_{min} between the maximum and the minimum transmitted intensity. The optimization criterion that we apply for the computer search is a trade off between these three conditions. We have performed two different computer searchs. On one side, we have considered the general approach where the magnitudes $\boldsymbol{h_1}$, $\boldsymbol{h_2}$, $\boldsymbol{j_1}$ and $\boldsymbol{j_2}$, are left as free parameters in the optimization process, and we use the two wave plates with a retardance of $2\boldsymbol{f_1} = 125$ degrees and $2\boldsymbol{f_2} = 94.5$ degrees at 458 nm. On the other side, we have considered the case $2\boldsymbol{f_1} = 2\boldsymbol{f_2} = 0$, corresponding to the situation when no wave plates are present. Then, we compare the results obtained for the classical system (only polarizers) and the general system with wave plates. In Table 2.4 we summarise the results obtained. We show the values for the intensity contrast ratio T_{max}/T_{min}, the minimum intensity transmittance T_{min}, and the variation of the phase-shift $\boldsymbol{D\psi}$.

Configuration		T_{max}/T_{min} ; T_{min} (%)		$D\gamma$ (degrees)	
		Predicted	Experim.	Predicted	Experim.
Only polarizers	j_1=91,j_2=89	198 ; 0.5%	∞ ; 0%	116	124
General	j_1=116,j_2=62 h_1=96,h_2=-7	100 ; 0.8%	61 ; 1.3%	33	18

Table 2.4. Predicted and experimental characteristic parameters for the amplitude-only configurations.

For the case of only polarizers, the optimization search leads to the polarizer transmission axis angles $j_1 = 91$ and $j_2 = 89$ degrees. The transmission axes of both polarizers are practically perpendicularly orientated to the director axis at the input and at the output face of the LCSLM respectively. This is the configuration that has been usually considered in the literature as the optimum one for amplitude-only modulation, as we simulated in Figure 2.9, Section 2.1.2.2. We note that the agreement between the predicted and the experimental parameters is very good for both configurations: only polarizers and general. An interesting result is that in all the cases the values for T_{min} are very low: close to 1%. In an amplitude-only configuration it is important to have a low value for T_{min}, because this energy contributes as a background noise.

We note that in display applications the main concern is to have a high contrast ratio, but in applications where amplitude-only modulation is required we also need a flat phase response. For the configuration with only polarizers the range of phase-shift is 124 degrees, which is far from a flat line. In the general case with wave plates, the amplitude-only modulation has been greatly improved with respect to the case with only polarizers because now the range of phase-shift is as low as 18 degrees while keeping good values for T_{max}/T_{min} and for T_{min}. The contrast ratio is lower but the minimum intensity transmittance is about 1%, which is a good value. An important result is that we have demonstrated that values as low as 18 degrees for the range of phase-shift are possible with a TN-LCSLM.

We note that the video projector is operating at brightness = 50 and contrast = 100. We mentioned in Section 2.2.4 that with these values the range of applied voltages is maximum because it goes from the saturation voltage to the Freedericksz voltage. This is the most suitable range to obtain phase-only modulation but it is the less suitable range to obtain amplitude-only modulation. The reason is that for a certain configuration of polarizing devices the phase-shift undergoes all the possible values, thus, we obtain the maximum range of variation of the phase-shift $\boldsymbol{D\psi}$. This fact gives more relevance to the good results we have obtained for the amplitude-only configuration in the general case with wave plates, where $\boldsymbol{D\psi}=18$ degrees while keeping good values for T_{max}/T_{min} and for T_{min}.

In Figure 2.32 we show the intensity and the phase-shift values over the gray levels applied for the only polarizers configuration and for the general configuration with wave plates. We show the experimental values (symbols) and the predicted curves (lines). Both in Figure 2.32 (a) and (b) we obtain an excellent agreement between predicted and experimental values. In Figure 2.32(a) we see that the evolution of the intensity transmission for the only polarizers configuration is not monotonous. However, for the general configuration with wave plates the evolution is monotonous and with a very linear slope.

In the general case with wave plates, we plot in Figure 2.33 the results for the amplitude-only configuration in the complex plane. As in Figure 2.31 we have normalized the amplitude transmittance to a maximum value of one. An ideal amplitude-only modulation is obtained when the measurements cover the Real axis from 0 to 1. We can see that the experimental points are practically overlapped along the whole positive side of the Real axis. Thus, this is a good amplitude-only configuration. The minimum amplitude transmittance is 0.11 that corresponds to the square root of the minimum value of the intensity transmittance displayed in Table 2.4, which is a very low value (1.3%).
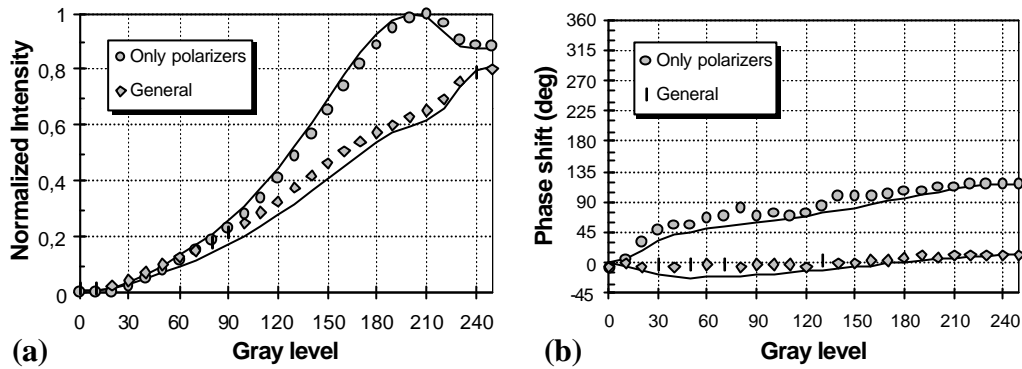
Figure 2.32. Amplitude-only modulation. Only polarizers and general configurations. (a) Normalized intensity. (b) Phase-shift. The symbols correspond to experimental measurements and the lines correspond to predicted values.
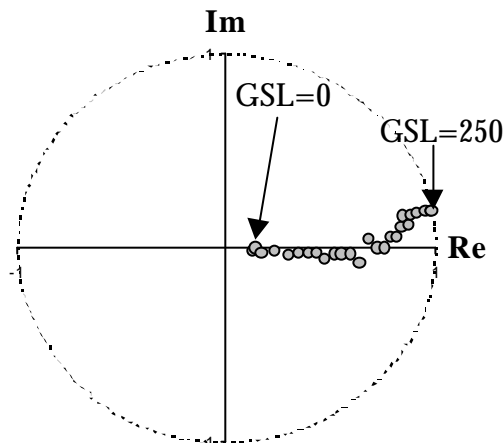

Figure 2.33. Complex plane representation of the amplitude-only modulation. The symbols correspond to the experimental measurements for the amplitude-only configuration in the general case with wave plates. The amplitude is normalized to a maximum value of one. The dashed line corresponds to a circle with unit radius.

In the different graphs presented along the present chapter of this thesis we have obtained an excellent agreement between experiment and prediction. The minor differences that appear can be partly explained because of the existence of interference and diffraction effects in the LCSLM, as shown by Davis *et al.* [Dav99c], which we have not included in the voltage dependent edge effect model.